# Fatigue properties of AlSi10Mg obtained by additive manufacturing: Defect-based modelling and prediction of fatigue strength

S. Romano [a], A. Brückner-Foit [b], A. Brandão [c], J. Gumpinger [c], T. Ghidini [c], S. Beretta [a],*

[a] Politecnico di Milano, Department of Mechanical Engineering, Via La Masa 1, I-20156 Milan, Italy
[b] Institute for Materials Engineering, University of Kassel, Moenchebergstrasse 3, D-34109 Kassel, Germany
[c] ESA/ESTEC, European Space Research and Technology Center, Keplerlaan 1, NL 2200AG Noordwijk, Netherlands

## abstract

Ability to predict the fatigue resistance of parts produced by additive manufacturing (AM) is a very current and frequently relevant open issue. The qualification of AM structural parts often needs a costly and time-consuming series of fatigue tests, on both samples and full-scale parts. Proper control of the AM process allows obtaining comparable and even better fatigue resistance than those obtained with standard manufacturing. Despite this, the experimental results often show a large scatter, mostly due to the presence of defects. In this framework, the present work summarizes the research activity aimed at modelling the high cycle fatigue (HCF) resistance in the presence of defects, focusing on AlSi10Mg produced by selective laser melting. Three batches of samples were investigated by X-ray micro computed tomography and tested under fatigue. A lower bound resistance curve was obtained, which introduced artificial defects of size corresponding to that of the largest occurring defects.

The analysis shows that a combination of defect-tolerant design with well-established and newly proposed fracture mechanics methods is the key to expressing the relationship between the fatigue strength and material quality. This is done through suitable statistics of material defects induced by the AM process.

The same concepts are then applied in a fatigue crack growth simulation model based on the maximum defect size, for estimating both the life and scatter of the data in the region of elastic material response. Based on this wide activity, it can be concluded that fracture mechanics-based analysis appears to be the tool needed for supporting the application of additive manufacturing to safety-critical components and their qualification.

Keywords:
AlSi10Mg
Computed tomography Additive
manufacturing Defects
Flaw tolerance Fatigue life assessment

---

* Corresponding author.
E-mail address: stefano.beretta@polimi.it (S. Beretta).

Published Journal Article available at: https://doi.org/10.1016/j.engfracmech.2017.11.002

## Nomenclature

| | |
|---|---|
| $a$ | crack depth |
| $da/dN$ | crack propagation rate |
| $d_g$ | sample gauge diameter |
| $f_N$ | Newman's closure function |
| $k_\sigma$ | inverse negative slope of the Wöhler curve before $N_{k,\sigma}$ |
| $k^*$ | inverse negative slope of the Wöhler curve after $N_{k,\sigma}$ |
| $l_g$ | sample gauge length |
| $r_g$ | sample gauge radius |
| $A_\%$ | percentage elongation after fracture |
| $C_n$ | parameter for fatigue strength assessment depending on material hardness and defect position |
| $C, n, p, q$ | NASGRO equation parameters |
| $F$ | cumulative distribution function |
| $K$ | stress intensity factor |
| $K_C$ | fracture toughness |
| $N_{k,\sigma}$ | knee point of the Wöhler curve |
| $R$ | stress ratio |
| $R_a$ | arithmetic average roughness |
| $R_{p,0.2}$ | 0.2% proof strength |
| $R_m$ | tensile strength |
| $R_z$ | average maximum peak to valley roughness |
| $V_g$ | specimen gauge volume |
| $V_{int}$ | fictitious internal gauge volume |
| $V_{surf}$ | fictitious surface gauge volume |
| $Y$ | boundary correction factor for SIF calculation |
| $\alpha$ | constraint factor |
| $\rho_u$ | density of the exceedances over the threshold $u$ |
| $\rho_{100}$ | density of the exceedances over 100 μm |
| $\sigma_{max}$ | maximum applied stress |
| $\sigma_{op}$ | crack opening stress |
| $\sigma_0$ | flow stress |
| $\Delta K$ | applied SIF range |
| $\Delta K_{th}$ | crack propagation threshold |
| $\Delta K_{th,eff}$ | effective crack propagation threshold |
| $\Delta K_{th,lc}$ | crack propagation threshold for long cracks |
| $\Delta\sigma$ | applied stress range |
| $\Delta\sigma_{def}$ | nominal applied stress range on the cross-section where the defect lies |
| $\Delta\sigma_{nom}$ | nominal applied stress range on the gauge volume |
| $\Delta\sigma_w$ | fatigue strength |
| $\Delta\sigma_{w0}$ | fatigue strength in absence of defects |
| $\sqrt{\text{area}}_{eff}$ | effective defect size |
| $\sqrt{\text{area}}_{max}$ | maximum defect size adopted in the fatigue crack growth simulations |
| $\sqrt{\text{area}}_{mean}$ | average defect size adopted in the fatigue crack growth simulations |
| $\sqrt{\text{area}}_{min}$ | minimum defect size adopted in the fatigue crack growth simulations |
| $\sqrt{\text{area}}_0$ | El-Haddad's size parameter |

*Acronyms*

| | |
|---|---|
| pdf | probability density function |
| AB | as-built (non-machined) parts |
| AM | additive manufacturing |
| CPCA | compression precracking constant amplitude |
| CT | X-ray micro computed tomography |
| EBM | electron beam melting |
| EPFM | elastic-plastic fracture mechanics |
| FCG | fatigue crack growth |
| HCF | high cycle fatigue |
| HT | heat-treated |
| LCF | low cycle fatigue |
| LEFM | linear elastic fracture mechanics |
| NDE | non destructive evaluation |
| POT | peaks-over-threshold maxima sampling |
| RO | run-out |
| SIF | stress intensity factor |
| SLM | selective laser melting |
| VO | vertical specimen orientation, upper position |
| VU | vertical specimen orientation, lower position |

## 1. Introduction

The aim of this research is to understand and model the fatigue resistance of an aluminium alloy produced by additive manufacturing (AM). This technology enables mass saving and allows producing components with very complex shapes. For space and aerospace applications, these shapes are often obtained by topological optimization, from a stiffness-driven design [1]. In addition to being the objective of optimization, stiffness is often the main requirement for these parts, which may be subjected to low stresses. Sometimes, however, different and more stressful loading conditions must also be considered, where the assessment of the finite-life fatigue resistance is the unique possibility. As an example, this could be the case for the launch phase of space components, where the loads and vibrations acting on parts could be high, but still in the high cycle fatigue (HCF) regime, whereas special parts such as fuel tanks have a service life in the low cycle fatigue (LCF) regime.

Today, AM is still limited to *minor* failure condition applications according to 14 CFR Part 25 Regulations for Transport Airplanes [2], which refer to applications in which safety must be significantly increased. However, the future of AM applications is gradually evolving to increased levels of part complexity and criticality, with a *major* failure condition (parts whose failure "…can affect the life-limited parts, including their life capability" [3]).

The new NASA standard for the qualification of AM parts for spaceflight [4] requires all the service parts to be manufactured together with a number of witness specimens for mechanical tests, such as tensile and fatigue tests, aimed at statistical process control. However, it is inconceivable that a complex part could be qualified with only a few tests, because the effective correspondence between these specimens and the final part must be confirmed [5].

In fact, in the authors' view, the key point for components is not the *material* & *process qualification* (which appears to be the main target of the NASA document), but rather the component assessment and verification that the unavoidable defects/inhomogeneities are not detrimental to the strength/life of critical component areas.

Companies and the AM user community would like to "avoid empirical (and potentially excessively) conservative system of safety factors to cover the risk of *unknown unknowns*" (quote from [6]). However, quick developments and improvements of the manufacturing processes make it impossible to keep pace with the production of expensive fatigue databases [7], and engineers require flexible tools for the *fitness-for-purpose* assessments. This is the topic of this study, in which the fatigue properties of different batches of AlSi10Mg samples produced by AM are analysed, whose processing has been significantly improved in the last three years. As it will be shown, a fracture mechanics approach is able to simply express the relationship between the HCF properties and material quality, which can be described by suitable statistics of the manufacturing defects' size [8] adopting the techniques developed for *extreme value* inclusion rating. An outlook of other applications of the same concepts is also discussed.

### *1.1. Fatigue properties of additively manufactured materials and defects*

The common denominator in fatigue results related to AM processes is the constant presence of significant scatter, particularly in the HCF regime and close to the material fatigue limit [9]. This scatter can be attributed to several variables affecting the nucleation and propagation of fatigue cracks, e.g., surface finish, defects, residual stresses, microstructure and anisotropy.

The primary variable affecting fatigue is surface finishing. As-built (unmachined) parts show a huge reduction of the fatigue properties, which can reach the order of 40% [10] for SLM (see Fig. 1) and up to 65% for EBM [11]. Several research groups in academia and industry are looking for solutions to this problem, e.g., by chemical or electrochemical etching [12], sand blasting, micro shot-peening, and vibratory polishing [13], or by laser ablation during the process [14]. At the same time, the producers of AM machines are constantly improving the final quality that can be obtained from the process [15,16].

Several works [9,10,17] have shown that manufacturing defects form an important class of variable in determining the fatigue limit of machined parts and which, at the actual state of the technology, are always present in AM parts. In fact, even if changing the laser parameters and adopting complex post-treatments (e.g., hot isostatic pressing) help reduce their number and size, it is never possible to completely eliminate this issue [9]. Moreover, these post-treatments usually require a huge amount of time and resources, thereby losing the beneficial effects of producing complex shapes with AM. Regarding defects, it should be considered that their position plays an important role [8,18]. In fact, the surface or subsurface defects are far more detrimental than the internal ones [9,19]. This is one of the variables explaining the intrinsic fatigue data variability, which can be in the order of 40–50% [20].

For a complete description of the fatigue strength, other secondary factors should also be considered. Among these, microstructure and residual stresses are the most important [5,7,9,21].

Under the hypothesis of a nearly homogeneous microstructure and low residual stresses, the influence of these variables becomes small with respect to that of the defects. Residual stresses can be relieved by post heat-treatments or sensibly decreased by imposing a controlled cooling by pre-heating the platform [17,22]. The role of microstructure is very important for crack propagation in the presence of very small defects and for energy dissipation during fatigue crack propagation.

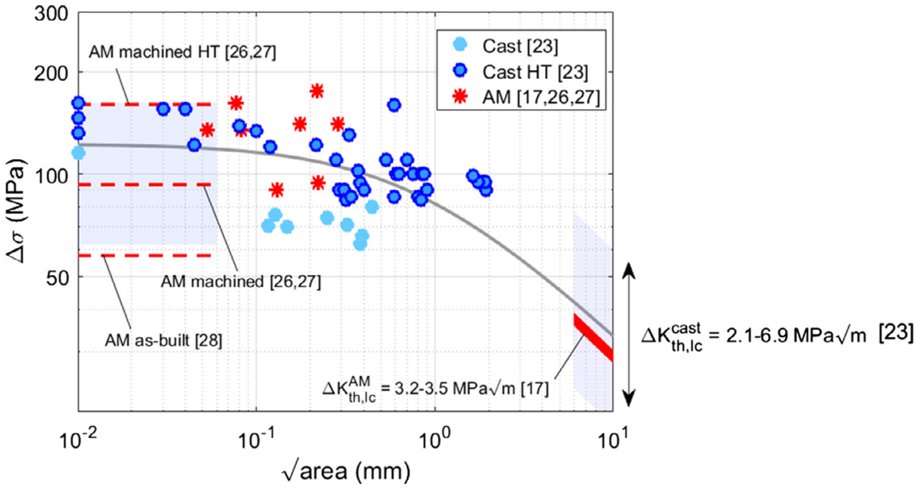

**Fig. 1.** Kitagawa diagram of AlSi10Mg alloy considering various literature data for cast [23] and AM [17,26–28] material at $R = 0.1$.

However, the fatigue limit is not sensibly affected by the microstructure when the defect size is larger than the grain size, especially in the case of ductile materials, which are typically less sensitive to impurities [9].

A literature review of two of the most used lightweight alloys in the space and aerospace sectors (AlSi10Mg and Ti6Al4V) [23] showed the applicability of the Kitagawa diagram [24] for assessing the fatigue limit of parts containing manufacturing defects. Fig. 1 shows that literature results related to AM processes are in line with (or even better than) data for cast parts. However, it can be seen that the data of cast Al show a definite trend when the defect size is considered. The scatter is a combination of the inherent variability and dependence on the defect size, which can be simply described by Murakami's $\sqrt{\text{area}}$ parameter [25].

In the case of cast Al, similar to AM-processed materials, thermal treatment dramatically improves the resistance with a vertical shift of the Kitagawa diagram of Fig. 1. One of the causes of this shift is the elimination of residual stresses as in [17]. A similar effect is also obtained with platform pre-heating. Moreover, as it can be expected from the Al literature [23], very small microstructural dimensions (owing to the fast cooling rates of the AM process) tend to increase the fatigue resistance in the absence of defects and decrease the long crack propagation threshold with respect to cast material [23].

Therefore, it appears that a proper fatigue strength description for AM materials should adopt the Kitagawa diagram and the concepts of *defect-tolerant design*, based on the experimental evidence of Murakami (summarized in [25]) that defects could be treated as short cracks at stress levels close to the fatigue limit.

Different researchers have pointed out the need for probabilistic defect-tolerant modelling in AM fatigue [5,7,29]. However, a systematic application of defect-based modelling of HCF fatigue properties (both life and fatigue strength) of a material processed by AM is still missing.

An important consequence of the adoption of defect-based modelling of fatigue strength, is that the strength of a material volume is controlled by the maximum defects present in the volume [30,31]. This led to the adoption of *extreme value statistics* as a support of design and quality control [32].

It has been shown that the same concepts can be easily applied to CT scans [8]. However, a common feature of AM is that failures are related to surface or subsurface inhomogeneities. It is therefore important to explain this experimental evidence. Moreover, the number of surface defects with respect to the embedded ones can be very large in topology-optimized parts, which often have a high surface-to-volume ratio. An explanation of the competitive role between surface and internal defects would allow consideration of only a small percentage of the flaws, which could be detected by CT scans and NDE, and to significantly reduce the computational effort required for crack propagation models.

### 1.2. Aims of this study

For the reasons explained so far, the present study presents a defect-tolerant assessment of the HCF properties of materials manufactured by AM, considering three series of AlSi10Mg manufactured by SLM. The aims of the research activity are summarised as follows:

- to demonstrate the strong connection between fatigue properties and defect content in the fatigue of machined AM specimens, highlighting the competition between surface and internal defects through a LEFM-based classification of the defects;
- to describe a *safe curve* for the fatigue strength assessment of AM parts based on a suitable description of the Kitagawa diagram and verify it by fatigue tests of specimens with artificial defects;

- to estimate the fatigue life and the scatter associated with experimental results by fatigue crack growth simulations based on the initial defect population determined through CT scans.

## 2. Experimental details

### 2.1. Material

The experimental activity was based on samples fabricated by SLM using the aluminium alloy AlSi10Mg. Five series of cylindrical fatigue samples were produced on an EOS M400 powder-bed machine between 2015 and 2017. The samples were produced by three processes, referred to as process 1 to process 3 (P1-P3). All the details about the material composition and manufacturing parameters adopted for P1 are reported elsewhere [8]. The same SLM machine, powder, and manufacturing parameters were adopted for P2. Therefore, no remarkable differences are expected between these processes. However, owing to the rapid development of SLM technology, the recirculating inert gas system required to remove released gas and particles was improved in the meantime. P3 was optimized with the aim of improving the fatigue resistance. The two parameters modified with respect to the previous processes were the layer thickness (reduced from 60 μm to 30 μm) and the platform pre-heating temperature (from 200 °C to 165 °C), see [13] for a more detailed description.

Two different orientations have been investigated, placing the specimen's axis parallel or perpendicular to the building direction. These will be referred to as vertical (V) and horizontal (H), respectively. Long vertical cylinders of material were built in P1, such that two samples per cylinder could be extracted on different heights with respect to the platform. In the following, the samples extracted from the bottom are called vertical under (VU), whereas those from the top are referred to as vertical over (VO). The aim was to assess any possible anisotropy developed during the manufacturing process, as highlighted considering resistance to fatigue crack growth, crack propagation threshold, and fracture toughness [5,7,9].

None of the parts received any final heat treatment; however, significant residual stresses were not expected owing to the platform pre-heating.

#### 2.1.1. Microstructure

The microstructure was analysed by observing polished cross-sections with optical microscopy, considering all the processes and orientations investigated. Chemical etching was performed, applying Keller's reagent for 10 s. The results are depicted in Fig. 2 and clearly show the shape of the melting pools, as well as the presence of some voids. The shape and dimensions of the pattern are inhomogeneous. No evident differences are visible between P1 and P2. The depth of the melting pools ranged between 60 and 140 μm, with a width of 70–230 μm. Despite the smaller layer thickness adopted (visible in the left image of Fig. 2c), P3 appears very similar to the previous materials, even if the number and size of the voids appear to be lower.

A very thorough review of the microstructure of a typical AlSi10Mg alloy manufactured by AM can be found in [33], whose material was very similar to the ones under investigation, including the size of the melting pools. It was found that inside the melting pools there is a fine microstructure constituted by *nanocells*. In [34] it was shown that the boundaries of the nanocells are decorated with eutectic AlSi phase, as it also happens for the borders of the melting pools. Given the pres-ence of such a fine microstructure, a short crack regime can be adopted when the size of detrimental defects is large enough (i.e. approximately larger than 100 μm), and therefore a fracture mechanics assessment of these defects is possible.

### 2.2. Computed tomography

The specimens for fatigue tests, the details of which are given in Section 2.4, have been subjected to a series of CT scans at ESTEC, in order to determine the prospective population of defects. The machine used for the X-ray CT scans of all the batches is a Phoenix V|tome|X m from General Electric (GE). The reconstruction was performed using the Phoenix datos-x software from GE, performing an optimisation for smoothing, beam hardening, ring artefacts, and post-alignment correction. All the post-processing, including the defect analysis, were performed using VG Studio Max 2.2.1 from Volume Graphics GmbH. The voxel size was set to 16 μm (see [8] for all the details).

The CT highlighted the presence of manufacturing defects in the bulk of all the batches and processes investigated. These defects appear to be randomly and homogeneously spread throughout the material. The manufacturing process usually causes two main defect types: gas porosity and lack of fusion [35]. To automatically distinguish the two defect types from the CT results is not an easy task, as both are characterised by a lower density than the bulk material. However, the two defect types can be distinguished by considering the shape, with porosity being almost spherical and lack of fusions being elongated along the manufacturing layer. Both were detected in all the samples investigated. Fig. 3 shows the defect distributions in a negative exponential probability plot. As already discussed for P1 [8], even for P2 and P3, the $\sqrt{\text{area}}$ projected perpendicularly to the manufacturing direction was seen to be the largest compared to the other projection directions. For this reason, the vertical samples are expected to be associated with the lowest fatigue resistance. At the same time, no evidence of clear differences between VO and VU samples was detected. A comparison of the distributions inside a vertical sample from every process is depicted in Fig. 3b. Figs. 3c and 3d show respectively the *sphericity* (measure for the ratio between the surface of a sphere with the same volume as the defect and the surface of the defect [36]) and the *shape ratio* of the

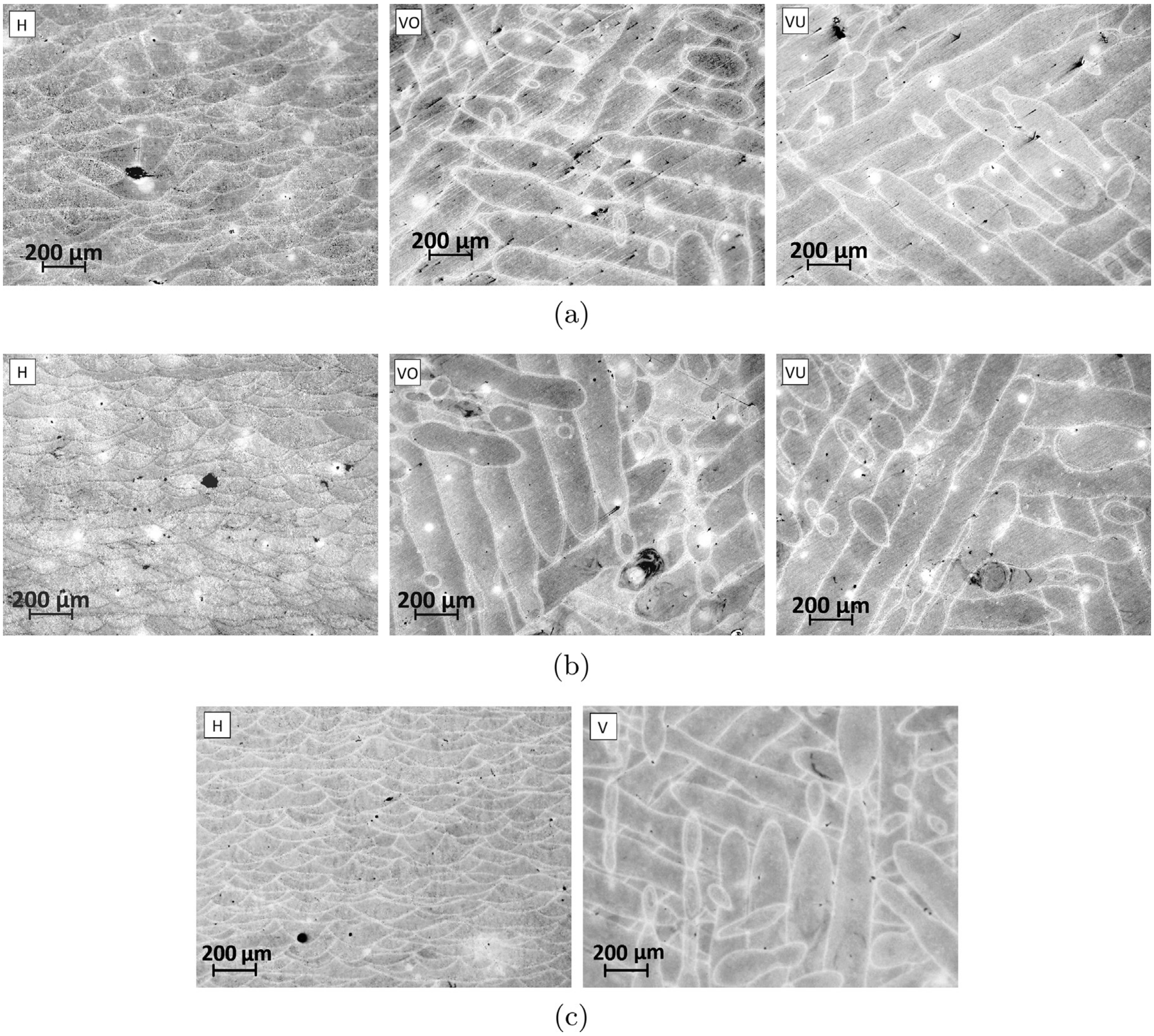

**Fig. 2.** Optical metallography after chemical etching for different material orientations: (a) P1; (b) P2; (c) P3.

bounding box containing the defects. These pictures give complementary information about the defect shape, showing the same trend for the three processes: all the largest defects are somehow elongated, as a confirmation that lack of fusion is the most dangerous defect type for the material investigated, as already discussed in [8] for P1.

Comparing the processes, P2 has the largest defect density (number of defects per unit volume), whereas P3 shows the lowest defect density (see Table 1). At the same time, the density of defects larger than 100 μm ($\rho_{100}$) decreases by almost 70% from P1 to P2 and by two orders of magnitude considering P3. Even if the overall density in P2 is larger than for P1, the lower number of large defects results in a much smaller maximum defect size. Looking at P3, the process improvements led to a sensible reduction of the overall number of defects. Moreover, the maximum defect size is again sensibly decreased to almost 100 μm in terms of $\sqrt{\text{area}}$.

The difference among the defect populations of three processes is important and its effect on fatigue properties will be discussed in Section 4. Note that, for a general definition of defect size in presence of large defect densities, the possible *clustering effects* could become a critical issue. This possibility has been investigated for P1 by implementing the interaction rules by Murakami [37] and its influence was seen to be negligible [8]. The analysis was also carried out for two samples of P2 and P3 obtaining similar results. This is the reason why this issue has not been considered while modelling of the behaviour of this material.

Finally, several high-density inclusions were detected in P2, whereas none of them was present in P1 and P3. Stoichiometric investigations have shown a composition of these inclusions compliant with aluminium oxides $Al_2O_3$. However, both the size of the maximum inclusion and the number of inclusions detected were smaller than those of the defects by approx-

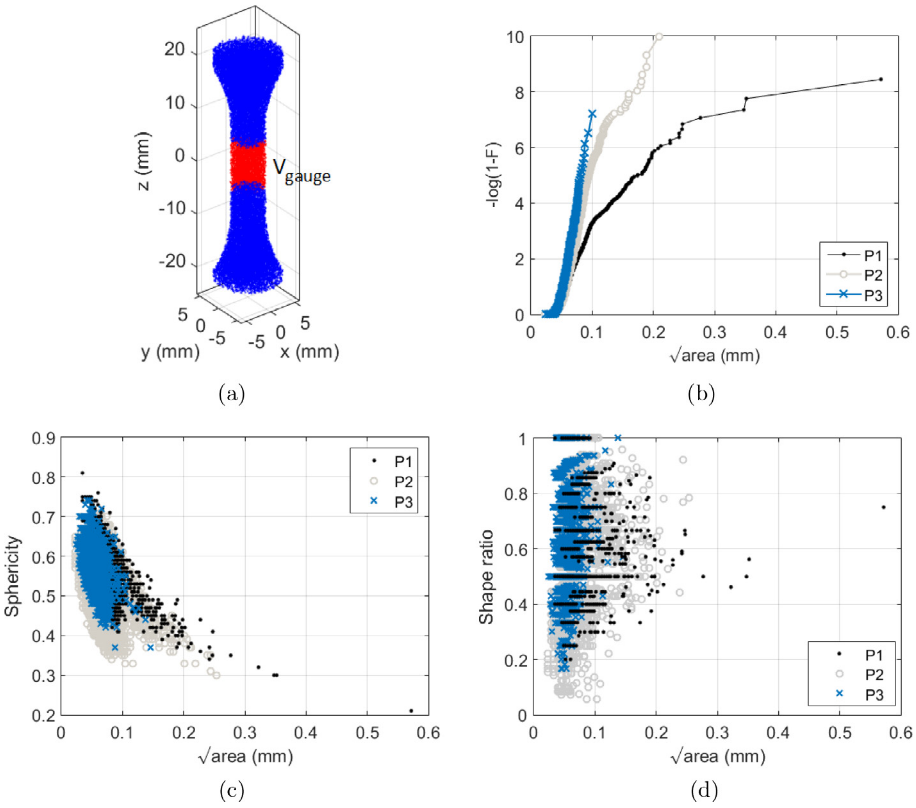

(a) (b)

(c) (d)

**Fig. 3.** CT scan results: (a) position of the defects detected in a sample, highlighting those inside the gauge volume; (b) comparison of defect distributions of a vertical sample in a negative exponential probability plot for the three processes investigated; (c) sphericity and (d) shape ratio as a function of the defect size.

**Table 1**
Summary of the defect densities measured by CT scan for the three processes.

| | P1 | | P2 | | P3 | |
|---|---|---|---|---|---|---|
| | average | std. dev. | average | std. dev. | average | std. dev. |
| $\rho$ (def/mm$^3$) | 10.8 | 3.6 | 23.8 | 16.7 | 1.9 | 0.7 |
| $\rho_{100}$ (def/mm$^3$) | 0.64 | 0.46 | 0.20 | 0.10 | $4.5 \cdot 10^{-3}$ | $3.1 \cdot 10^{-3}$ |

imately 30–35% and 90–97%, respectively. Their influence on the fatigue performance of the samples can therefore be expected to be relatively small.

### *2.3. Basic mechanical properties*

Tensile tests have been performed at room temperature, according to DIN EN ISO 6892 [38]. The machine used was an MTS RT 100 equipped with a 100 kN load cell. The testing speed was set to 2 mm/min.

The results of the static tests are reported in Table 2. No particular differences were highlighted between the vertical samples manufactured at different heights. Therefore, the unique distinguishing factor was sample orientation. The data show an increase in both the yield stress $R_{p,0.2}$ and ultimate tensile stress $R_m$ between P1 and the other two processes. At the same time, the variability between the different samples decreased, confirming the process improvement. In all cases, these static properties outperform those obtainable by casting. Even the maximum strain at failure is quite good, reaching 6.4–7.2% for the horizontal samples and slightly lower values for the vertical orientation.

The cyclic response of the material was investigated performing axial strain-controlled tests on an MTS 810 servohydraulic machine, with a frequency of 0.5 Hz. A stress ratio $R = -1$ was applied and the strain was measured using a clip-on gauge extensometer. The stabilised hysteresis loops for various deformation levels were then collected and a Ramberg-Osgood [39] equation was fitted to these data. The cyclic yield stress, $R^c_{p,0.2}$, is summarised in Table 2. The clear trend is a progressive increase in the cyclic yield stress when the process is improved, as well as a higher resistance of

**Table 2**
Summary of the tensile and cyclic properties.

| Process | Orientation | | $E$ (GPa) | $R_{p0.2}$ (MPa) | $R_m$ (MPa) | $A_{\%}$ (%) | $R^c_{p0.2}$ (MPa) |
|---|---|---|---|---|---|---|---|
| P1 | horizontal | average | 73.3 | 224.9 | 365.3 | 6.8 | 191.8 |
| | | std. dev. | 0.4 | 4.8 | 4.9 | 0.4 | |
| | vertical | average | 72.6 | 236.3 | 406.4 | 5.3 | 217.6 |
| | | std. dev. | 0.2 | 16.7 | 5.0 | 0.4 | |
| P2 | horizontal | average | 74.6 | 304.5 | 441.5 | 6.7 | 225.8 |
| | | std. dev. | 0.1 | 0.7 | 0.7 | 0.1 | |
| P3 | horizontal | average | 70.2 | 291.0 | 443.7 | 6.6 | 232.8 |
| | | std. dev. | 1.8 | 3.8 | 3.2 | 0.4 | |
| | vertical | average | 72.8 | 253.7 | 440.2 | 3.0 | 211.4 |
| | | std. dev. | 2.3 | 2.3 | 4.9 | 0.2 | |

**Table 3**
Summary of the tests performed.

| Process | Tensile | FCG | HCF |
|---|---|---|---|
| P1 | 6 | | 18 |
| P2 | 2 | 4 | 45 |
| P3 | 6 | | 42 |

the vertical orientation with respect to the horizontal. For more information, some results and modelling related to P1 can be found in [40].

## 2.4. Fatigue tests

The S-N curve was characterised by a series of axial force-controlled tests and the crack propagation rate was measured by fatigue crack growth (FCG) tests. The number and type of tests performed are reported in Table 3.

A common observation for SLM is that as-built parts show a significant reduction in fatigue resistance compared to that in machined parts. This reduction can be on the order of 40–50% considering a technically relevant fatigue strength of $2 \cdot 10^6$ cycles, depending on the final surface quality (see [9,20,23]). As the aim of this study is the assessment of AM parts in relation to the presence of internal manufacturing defects, all the specimens have finally been machined. The final surface roughness was measured with a profilometer, yielding $R_a = 0.33$ μm and $R_z = 2.99$ μm.

All the fatigue samples were designed according to ASTM E606 [41]. The geometry of the cylindrical specimens is reported in Fig. 4a, and the important dimensions (such as gauge length $l_g$, diameter $d_g$ and volume $V_g$) are summarised in Table 4. Although the different batches produced have slightly different dimensions, the gauge volume of all the specimens is between 201 mm$^3$ and 452 mm$^3$; therefore, no visible volume effect is expected.

Fatigue experiments were carried at R = $-1$. These tests were jointly performed by ESTEC & PoliMi. The tests at ESTEC were carried out on an Instron ElectroPuls E10000 machine equipped with a 10 kN load cell, by applying a frequency of 30 Hz. The tests at PoliMi were performed on an MTS 810 servohydraulic machine (capacity 100 kN) at a frequency of 15 Hz.

### 2.4.1. Tests with artificial defects

A common observation in literature is that the fatigue failure of AM samples is generally caused by surface or subsurface voids [8,9,18,20]. To define a safe reference fatigue life curve, artificial micronotches were introduced in the gauge volume of some samples. Applying the concepts described in [8], the area of the artificial defects was determined as a safe percentile (i.e., 97.5%) of the maximum defect distribution in the surface gauge volume (see Section 4.2).

For specimens P1, the size of this defect resulted $\sqrt{area} = 500$ μm. The micronotches were introduced by milling in the centre of the specimen gauge length (see a detail in Fig. 4b). The real dimensions, determined after the failure of samples, were slightly smaller, with an average of 374 μm and a standard deviation of 55 μm. The same was done for P2 and P3 but, owing to the smaller defect sizes in the material, the micronotches were produced by femtosecond laser ablation with the techniques and geometry described in [42]. This process rapidly brings very small volumes of material from the solid state to the gas/plasma state. The very high frequency and low exposure time do not allow heat conduction, thus avoiding the formation of large heat-affected zones. The energy was set to 5–8 μJ. The 97.5% sizes for P2 and P3 were calculated as 260 μm and 150 μm, respectively. The meaningful geometric parameters are reported in the sketches of Fig. 4c and d. The measurements after the tests highlighted a larger dimension than expected considering P2, with an average increase in size of 290 μm and a scatter of nearly 20%. As for P3, the average size obtained resulted in agreement with the target dimension, with a standard deviation of 10%.

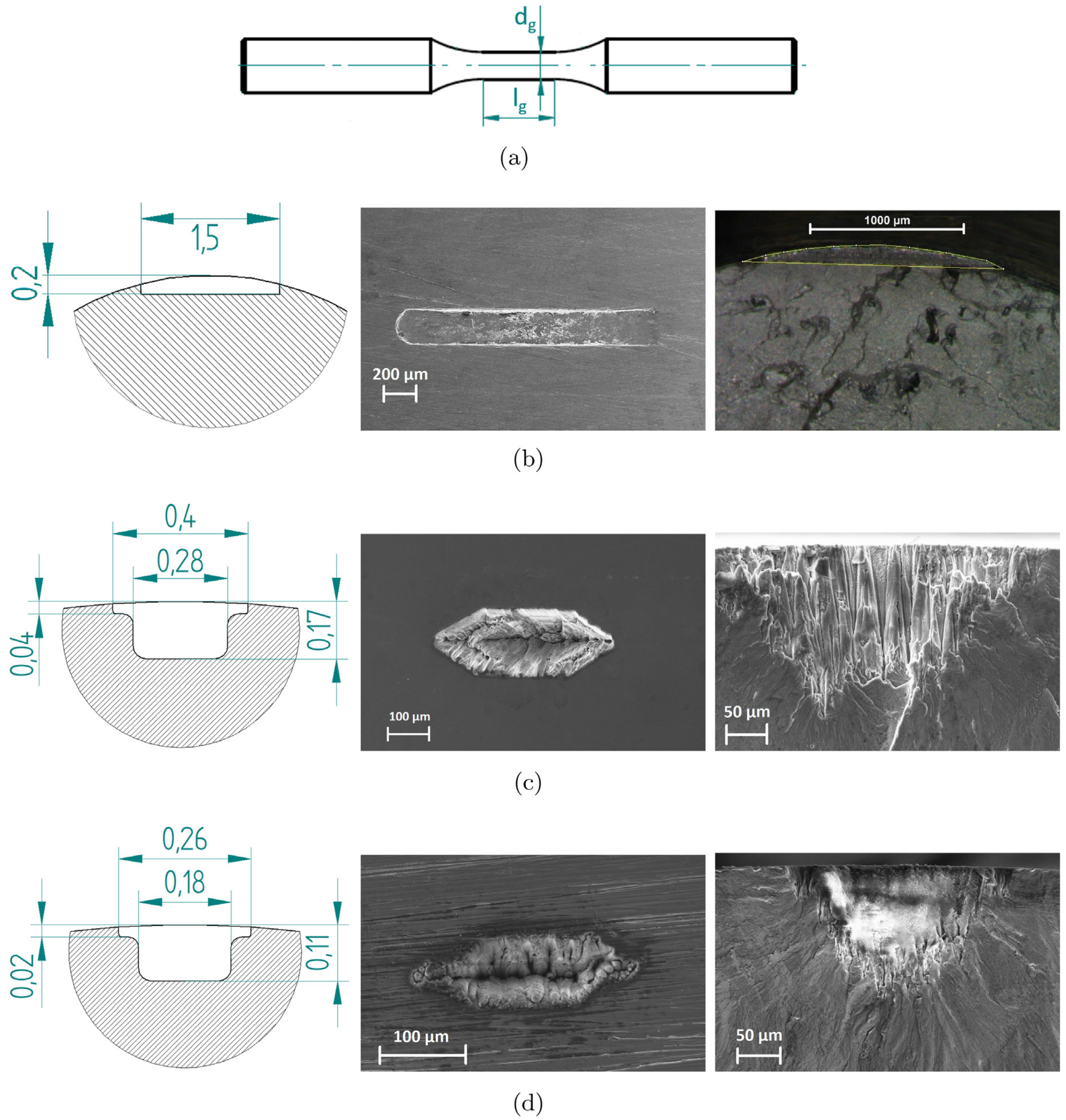

**Fig. 4.** Geometry of the fatigue samples: (a) scheme of the cylindrical specimens and gauge dimensions; Detail of the artificial defects introduced for (b) P1, (c) P2 and (d) P3.

**Table 4**
Summary of number and dimensions of the samples produced.

| Process | Number of samples | $d_g$ (mm) | $l_g$ (mm) | $V_g$ (mm$^3$) |
|---|---|---|---|---|
| P1 | 12 | 5.1 | 13 | 266 |
| | 30 | 6.0 | 16 | 452 |
| P2 | 58 | 6.0 | 16 | 452 |
| | 14 | 4.0 | 16 | 201 |
| P3 | 76 | 5.5 | 11 | 261 |

### 2.5. Fatigue crack growth

FCG in the absence of crack closure was investigated by fatigue crack propagation tests on two compact tension (C(T)) specimens from P2 at a stress ratio $R = 0.7$. The intrinsic anisotropy of the manufacturing process involves a dependency of the resistance to fatigue crack propagation with respect to the loading direction [5,9,35,43]. For this reason, the most detrimental crack propagation direction (i.e., crack parallel to the manufacturing layer) was investigated. This hypothesis matches with the propagation in the vertical samples, whereas a slightly conservative life assessment is expected for the horizontal samples. The samples were designed and tested according to the standard (C(T)) specimens [44], with a width of 12.7 mm on a MTS 810 test servohydraulic machine. After a compression precracking for $10^6$ cycles at a stress ratio $R = 10$, a constant amplitude loading was applied to determine the FCG curve up to the final failure. The frequency was set to 15 Hz. The crack advance was measured by a clip-gauge and verified at the end of the test by measuring the final crack length on the fracture surface.

Other tests were also carried out on the P2 process at Kassel University, in order to precisely measure $\Delta K_{th}$ at $R = -1$. In detail, single edge notched tensile specimens with a dimension of 12 mm × 4 mm were first machined with EDM to produce a semi-circular notch with a radius of approximately 0.2 mm and a depth of 0.3 mm. Subsequently, a very sharp initiation point was introduced by razor blade. Finally, the specimens were subjected to compression precracking and then tests with the CPCA technique [45] to determine $\Delta K_{th}$. These tests were carried out on a resonant axial test machine with a capacity of 100 kN, at a frequency of 150 Hz. The crack advance was measured with a Hirox optical microscope, using a magnification of 210×. After compression precracking, the specimens were subjected to a starting $\Delta K$ value above $\Delta K_{th,eff}$ and a constant cyclic load was applied. After an initial crack growth, the crack stopped (average speed $da/dN < 10^{-11}$ m/cycle for at least $10^6$ cycles) owing to crack closure development. After the crack stopped, the load was increased so that the initial applied $\Delta K$ for the next step overcame the final one of the previous step by 0.3–0.4 MPa $\sqrt{\text{m}}$. This procedure was repeated step-by-step up to $\Delta K$ values above the crack propagation threshold for fully-developed crack closure at $R = -1$, where crack propagation became stable. This technique also allows to obtain the so-called *cyclic R curve* considering all the $\Delta K$-$\Delta a$ values measured at the end of every step [46–49].

## 3. Test results

This section summarises the results of the fatigue tests performed and aims at explaining and understanding the material behaviour and the differences noticed among the different investigated processes.

### 3.1. Defects at the fracture origin

All the fracture surfaces were analysed after the fatigue failure. Images were taken with a stereo microscope to gain an overview of the fracture surfaces, whereas deeper investigations were conducted through the SEM, see Figs. 5 and 6.

As can be seen from the images shown in Fig. 5, both the horizontal and vertical samples present irregularly shaped defects, sometimes still containing powder particles (see Fig. 5c), and therefore such defects are called lack of fusion [50]. For the AM material, this peculiar defect typically has a flat shape and is oriented parallel to the horizontal (x-y) plane [51].

Ahead of the defects, in some vertical specimens there were traces of *spatter ejection* [52] (see Fig. 5a). The texture of these regions appeared to be *solidified material*, see Fig. 6, and it was therefore different from surface texture of fatigue crack growth surface. When this defect is observed through the backscattered electrons (BSE) detector, tiny cracks along the spat-ter ejections are revealed (Fig. 6c).

The size of the defect at the origin of failure, hereinafter referred to as *killer*, was measured in terms of the $\sqrt{\text{area}}$ parameter. The *effective size* was determined based on the guidelines described by Murakami [25,37], which give good results, even applied to AM defects [53].

### 3.2. High cycle fatigue resistance

The results of the fatigue tests are summarised in Fig. 7a. As it could have been expected from the defect distributions, the vertical samples generally show a slightly lower life than the horizontal samples. In fact, the average difference in terms of life between the horizontal and vertical orientations is less than 5% for P1, but it becomes nearly 23% considering P2 and 28% for P3. However, no visible differences were detected between vertical samples placed in different positions of the job volume. As a general observation, the life variation due to the defect orientation is definitely negligible if compared to that between different processes. Therefore, the entire process has been described by a unique symbol in order to clarify the picture readability. Considering the different processes, the gap between P1 and P2 is quite evident. As no microstructural differences were detected between the samples, this can be primarily attributed to the size of the defects leading to failure. A further improvement was achieved with P3, for which the main improvement can again be attributed to the decrease in the maximum defect size, as shown by the progressive reduction of the killer dimension from P1 to P3 in Fig. 7b. This reduction reflects the trend clearly indicated by the CT results of Fig. 3.

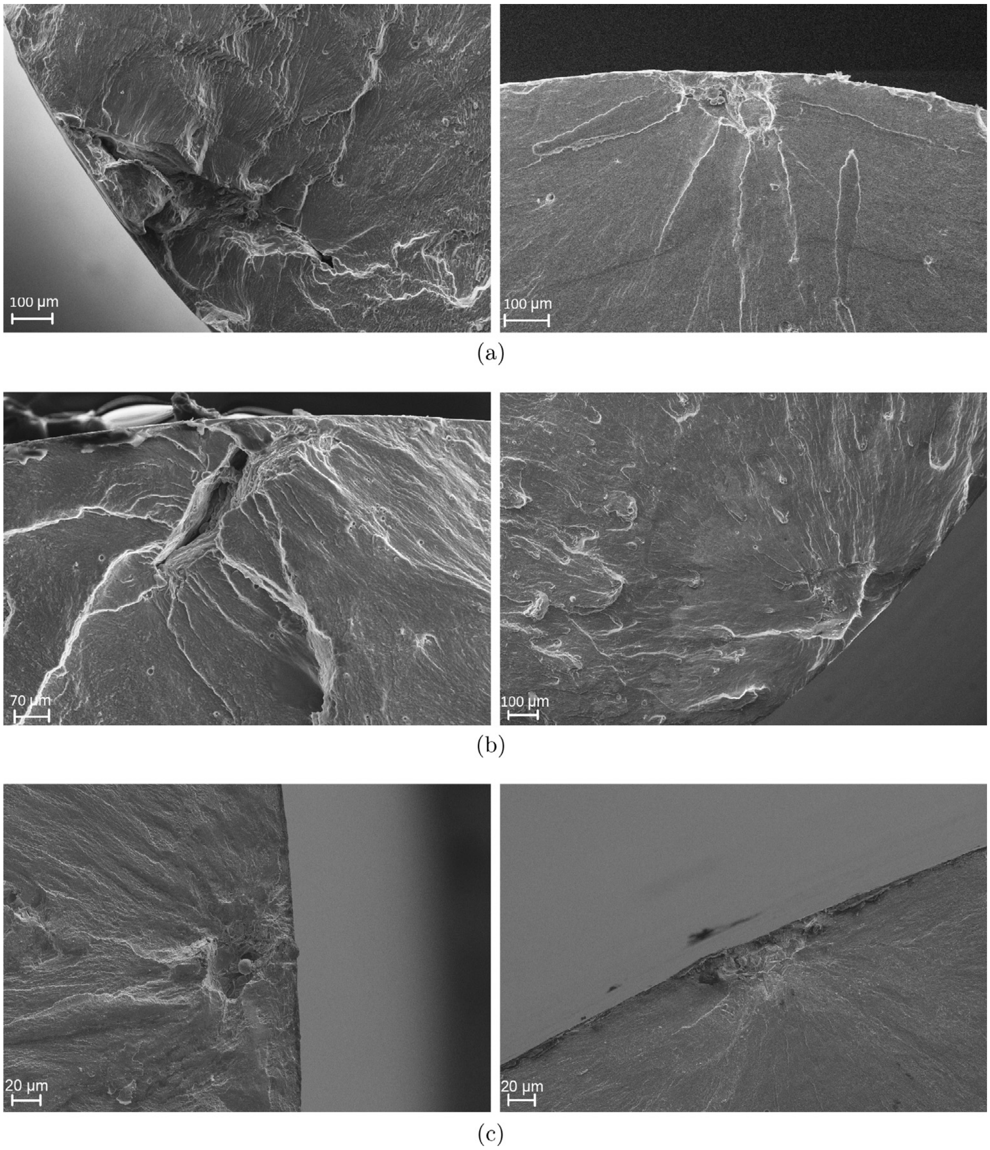

**Fig. 5.** SEM observation of the killer defects found in horizontal (left column) and vertical (right column) specimens of: (a) P1; (b) P2; (c) P3.

The estimation of the size of the *killer defects* through the analysis of the CT scans will be the topic of Section 4.2. The estimates related to the three batches are shown in Fig. 7b as a box defining the 2.5% and 97.5% percentiles, whereas the horizontal line shows the average value of the Gumbel distribution.

Two important conclusions can be drawn, which may be helpful during the design and testing phases:

- the presence of large defects not only decreases the fatigue resistance of the material, but also increases the scatter associated with the Wöhler curve;
- the artificial defects introduced outline a safe lower bound curve with low scatter. The adoption of this S-N curve could allow one to obtain a safe design with both high confidence and limited effort in terms of the time and number of specimens required.

### *3.3. Crack growth tests*

Fig. 8 summarises the results of FCG tests, which have been performed on the material manufactured by P2. The Paris equation was fitted to the linear part of the data of two C(T) samples, up to 70% of the maximum SIF at failure. Adopting

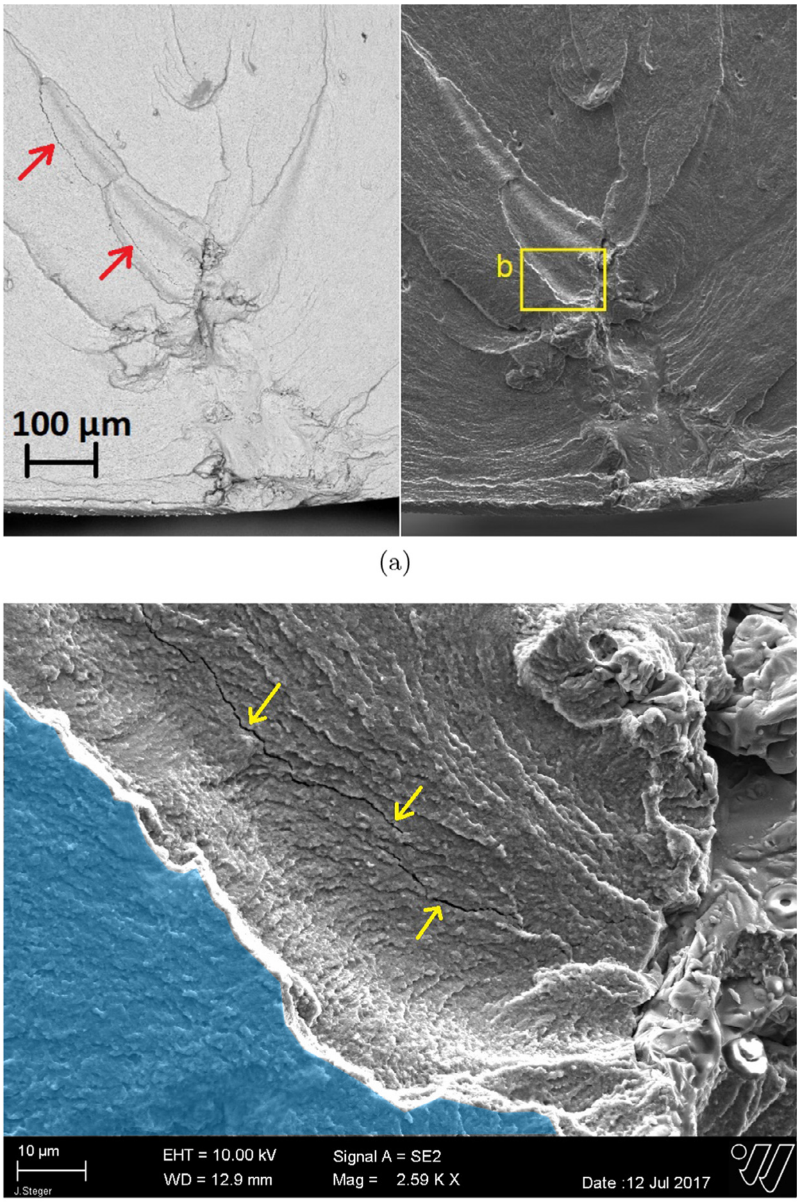

(a)

(b)

**Fig. 6.** SEM image of the killer defect of a vertical sample from P2 containing microcracks (arrows) in the region of spatter ejection ahead of the defect: (a) backscattered and secondary electrons mode; (b) detail of a small region (crack propagation region highlighted in light blue, see the web version).

Newman's model [54], the FCG data obtained for a stress ratio $R = 0.7$ allowed to estimate the growth rate at the stress ratio of interest, $R = -1$.

The results of the CPCA tests provided two $\Delta K_{th,lc}$ values of 3.2 and 3.6 MPa $\sqrt{m}$. The crack growth rate data above $\Delta K_{th,lc}$ are in good agreement with the closure-corrected Paris curves (see Fig. 8). The theoretical estimates of $\Delta K_{th,eff}$ obtained from the Young's modulus [55] and the Burger vector [56] ($\Delta K_{th,eff} = 1.18 - 1.26$) are shown in the same picture. This estimated $\Delta K_{th,eff}$ is consistent (again considering the Newman's closure correction) with the experimental results. It is worth pointing out that $\Delta K_{th,lc}$ experimental results for P2 lie in the lower bound of the threshold range for AlSi10Mg produced by standard manufacturing [23] (see Fig. 1). The tests performed show a limited variability of the FCG rate for P2, in contrast to the fatigue properties, which are highly dispersed owing to the manufacturing defects.

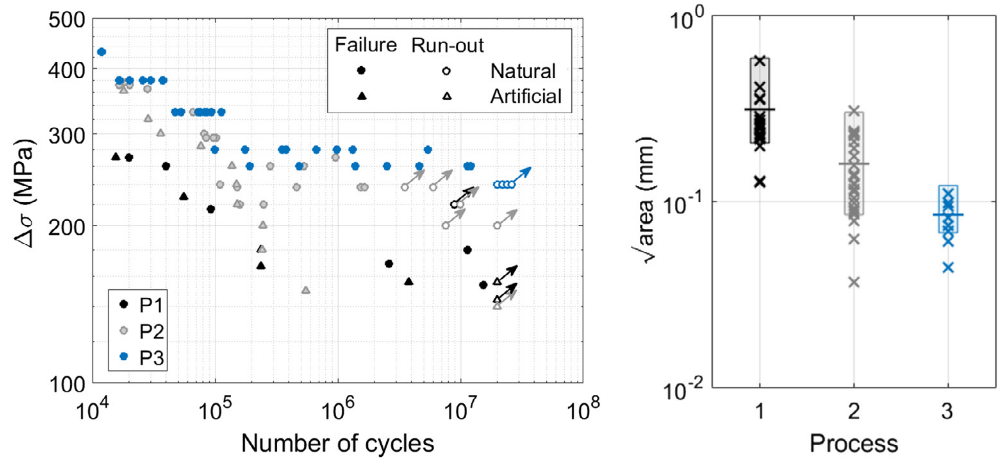

(a) (b)

**Fig. 7.** Experimental fatigue results ($R = -1$, frequency 15 Hz): (a) S-N curve; (b) dimension of killer defects (box plots refer to the size estimated by the analysis of CT scans, see Section 4.2).

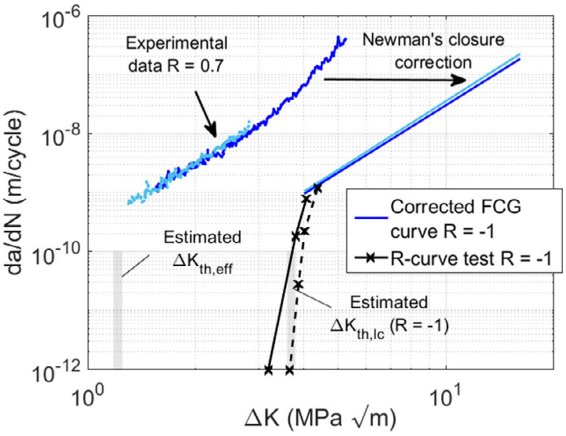

**Fig. 8.** Fatigue crack growth tests on P2.

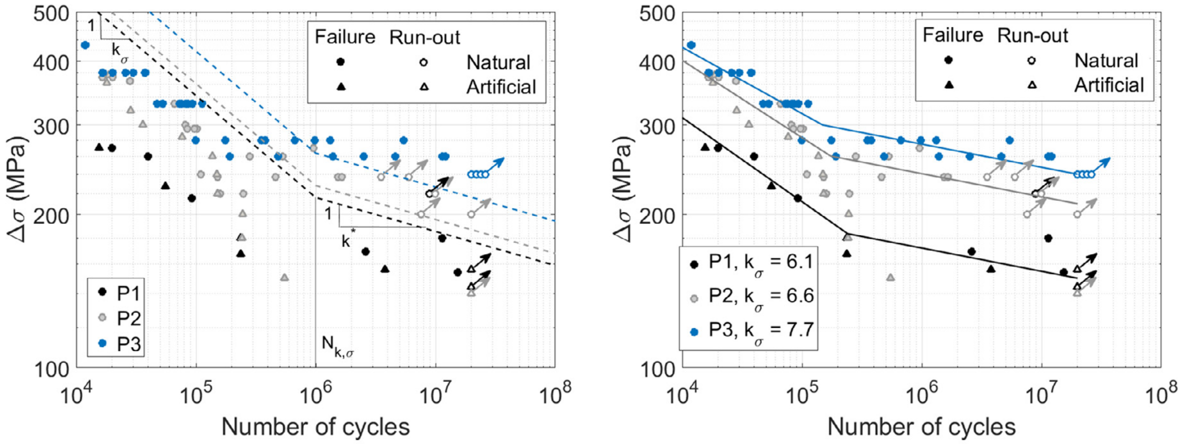

(a) (b)

**Fig. 9.** Assessment of the Wöhler curve: (a) FKM guideline, (b) experimental fit.

## 4. Discussion

### 4.1. S-N diagram

Despite the clearly different fatigue resistances among the three processes, the slope of the Wöhler curves does not appear to change significantly. For cast aluminium alloys, the FKM guideline [57] reports a slope $k_\sigma = 5$ before $N_{k,\sigma} = 1 \cdot 10^6$ cycles and a slope of $k^* = 15$ after this knee point. The stress amplitude at the knee point can be estimated as 30% of the ultimate tensile strength. Fig. 9a shows that this guideline does not correctly describe the present data, result-ing in an overestimation of the fatigue resistance. In fact, the experimental negative inverted slope is in the range $k_\sigma = 6.0 - 7.7$, whereas $k^*$ suddenly increases significantly after approximately $N_{k,\sigma} = 2 \cdot 10^5$ cycles (see Fig. 9b). For the following analyses, a value $k^* = 22$ was derived by fitting the data over $N_{k,\sigma}$. This value is consistent with that used by Sonsino [58,59] for similar cast materials.

This deviation from the standard properties of aluminium alloys is not surprising, considering other literature results for the same material produced by SLM. Brandl et al. [26], for example, report a $k_\sigma$ value similar to that proposed by FKM, but a knee point at $N_{k,\sigma} = 2 \cdot 10^5$ cycles as in the present case. The results by Mower [10], however, show a slope $k_\sigma$ close to 6.2, not far from the present results.

In a summary, an unambiguous determination of the single S-N curve slopes is almost impossible, considering that the fatigue strength at 10 million cycles ranges between 150 MPa and 240 MPa and this scatter appears to be controlled by the manufacturing defects, which are very different between P1 and P3. In this scenario, on the one hand, the fatigue design should adopt unreasonably large safety factors, while on the other hand, it would be worth adopting a robust *predictive framework* that would allow designers to quickly estimate design limits and update them as a consequence of the rapid process improvements. This topic will be thoroughly discussed in Section 5.1.

### 4.2. Stress intensity factor at the fracture origin

In [8] the authors have demonstrated that, for the particular batch of material investigated, the maximum defect within a volume can be correctly described by adopting the statistics of extremes. These results can be used to infer the fatigue resistance, under the hypothesis that the largest defect is that at the origin of failure. This assumption is commonly adopted in industrial applications, but it may not be true in the present case. In fact, it is well known that surface defects are far more detrimental than internal defects, because of which one can expect crack propagation to originate from the surface, even in the presence of a larger embedded defect. The predominance of failures originating from the surface is a very common observation in the presence of defects, and particularly in AM applications [9,18,20].

The same evidence was confirmed experimentally: the failures originated from the surface or from subsurface defects (see Section 3.2), except for two failures. Both of these failures belong to P1 and were caused by very large areas of lack of fusion.

Considering the CT scan of fatigue specimens, there are no data supporting the evidence of larger defects close to the surface. On the contrary, the spatial defect distribution appears to be homogeneous, thus confirming the importance of this *surface effect*. Although its influence may be negligible for massive components, it can be relevant when the external surface becomes large with respect to the volume, which is the case for most AM applications. When dealing with fracture mechanics, what matters is not only the applied stress and the crack size, but also the *driving force* that makes the crack propagate. Considering defects, the SIF range $\Delta K$ can be described with Murakami's formula [37,60]:

$$\Delta K = Y \cdot \Delta\sigma\sqrt{\pi\sqrt{area}} \tag{1}$$

where $Y = 0.5$ for internal defects and $Y = 0.65$ for surface defects. Note that, for the same defect size, the difference in the applied SIF is on the order of 30% and therefore an internal defect with the same $\Delta K$ should have a size 70% larger than a surface defect. Assuming a circular defect shape to simplify the problem, an empirical rule by Murakami [25] can be used to classify a defect as superficial when Eq. (2) is verified:

$$a/h > 0.8 \tag{2}$$

where $a$ is the radius of the equivalent circle and $h$ is the distance between the defect centre and the external specimen surface (see Fig. 10a). Moreover, the definition of an *effective defect size* for a correct SIF calculation is required when the defects lie below the surface, as in Fig. 10b [25,53].

To verify whether the SIF calculated using Eq. (1) is an appropriate variable to assess how detrimental a defect could be, this relationship was used before the testing to calculate the SIF of all the defects detected by CT. In this way, it was possible to rank the defects according to their SIF and to foresee which defect would have caused the fatigue failure according to this hypothesis. After the tests, the predictions based on the SIF were verified by searching for the real killer among the CT measurements. Five samples randomly chosen from P1 were investigated and the results are summarised in Table 5. Note that there is a third variable to be considered apart from $Y$ and $\sqrt{area}$, which is the stress acting on the defect, $\Delta\sigma_{def}$, calculated as

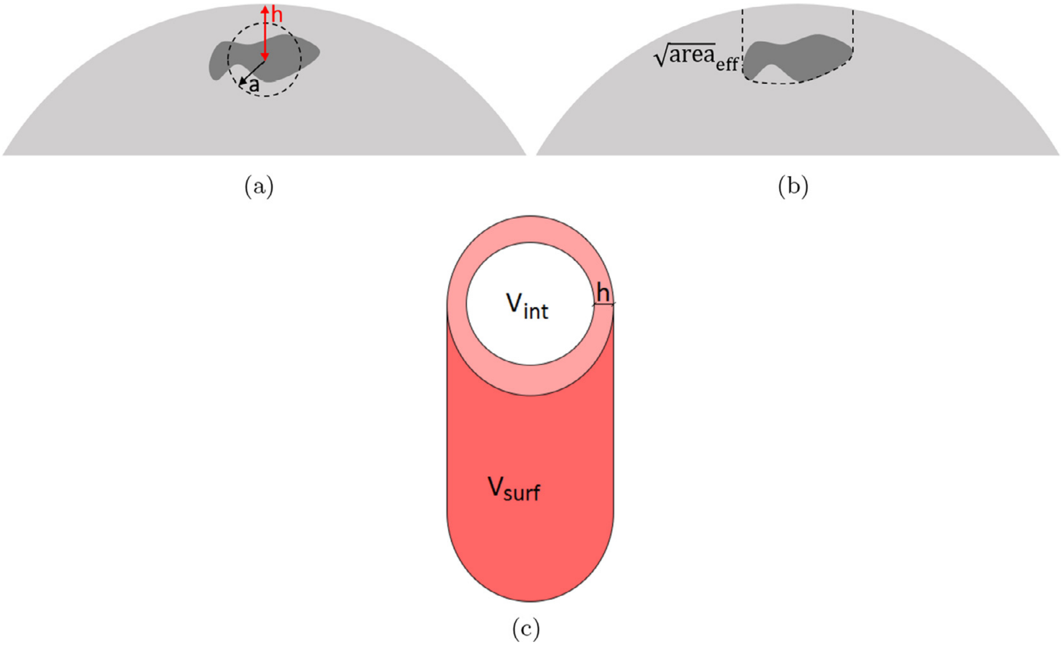

**Fig. 10.** Scheme for the analysis of defects: (a) equivalent circular defect and distance from the surface, (b) area increment for subsurface defects, (c) *equivalent surface volume* associated with the specimens.

**Table 5**
Summary of the SIF ranking investigation on 5 specimens randomly selected from P1.

| Specimen name | $\Delta\sigma_{nom}$ (MPa) | SIF rank | $\sqrt{area}$ ($\mu m$) | $\Delta\sigma_{def}/\Delta\sigma_{nom}$ | Position | $\Delta K$ (MPa$\sqrt{m}$) | Killer |
|---|---|---|---|---|---|---|---|
| H02 | 220 | 1 | 272 | 1.00 | surface | 4.18 | × |
| | | 2 | 202 | 1.00 | surface | 3.60 | |
| | | 4 | 295 | 1.00 | embedded | 3.35 | |
| H03 | 360 | 1 | 209 | 1.00 | surface | 5.99 | |
| | | 2 | 169 | 1.00 | surface | 5.39 | × |
| | | 3 | 283 | 1.00 | embedded | 5.36 | |
| VO01 | 200 | 1 | 572 | 1.00 | embedded | 4.24 | × |
| | | 2 | 242 | 0.99 | surface | 3.55 | |
| | | 3 | 297 | 0.88 | surface | 3.51 | |
| VU02 | 180 | 1 | 437 | 0.99 | surface | 4.31 | × |
| | | 2 | 414 | 0.91 | surface | 3.86 | |
| | | 4 | 470 | 1.00 | embedded | 3.46 | |
| VU03 | 295 | 1 | 223 | 1.00 | embedded | 3.91 | |
| | | 2 | 129 | 1.00 | surface | 3.86 | × |
| | | 3 | 214 | 1.00 | embedded | 3.83 | |

the nominal stress applied to the cross-section. In fact, the ranking even considered even the defects in the grip regions, where the applied stress is lower than the nominal stress $\Delta\sigma_{nom}$.

From the analysis presented, it is evident that the prediction is precise and robust. In fact, in all five cases, the failure originated from the first or second defect ranked in terms of SIF. The ranking was able to predict a surface failure in the presence of larger embedded defects (H02-H03-V02U-V03U), but also failures originated from internal defects (V01O) and from outside the gauge volume (V02U). It should be noted that these predictions could be further improved by considering more complex models (e.g., accounting for the defect features). However, the result is surprising if one thinks that the defects reported for every sample were selected from several tens to thousands of measurements considering only three easily measurable variables.

The competing risk between surface and embedded flaws is depicted in Fig. 11, comparing the size and SIF distributions. In detail, defects at the fracture origin for the P1 process were interpolated with Gumbel distributions (killer defects, only surface killers, internal killers): one would expect most of the failures to originate from the internal volume of the sample (as it is larger than the surface), as depicted in Fig. 11a and c. On the contrary, this is not the case when the SIF distribution is considered (see Fig. 11b and d): the SIF is larger for surface defects.

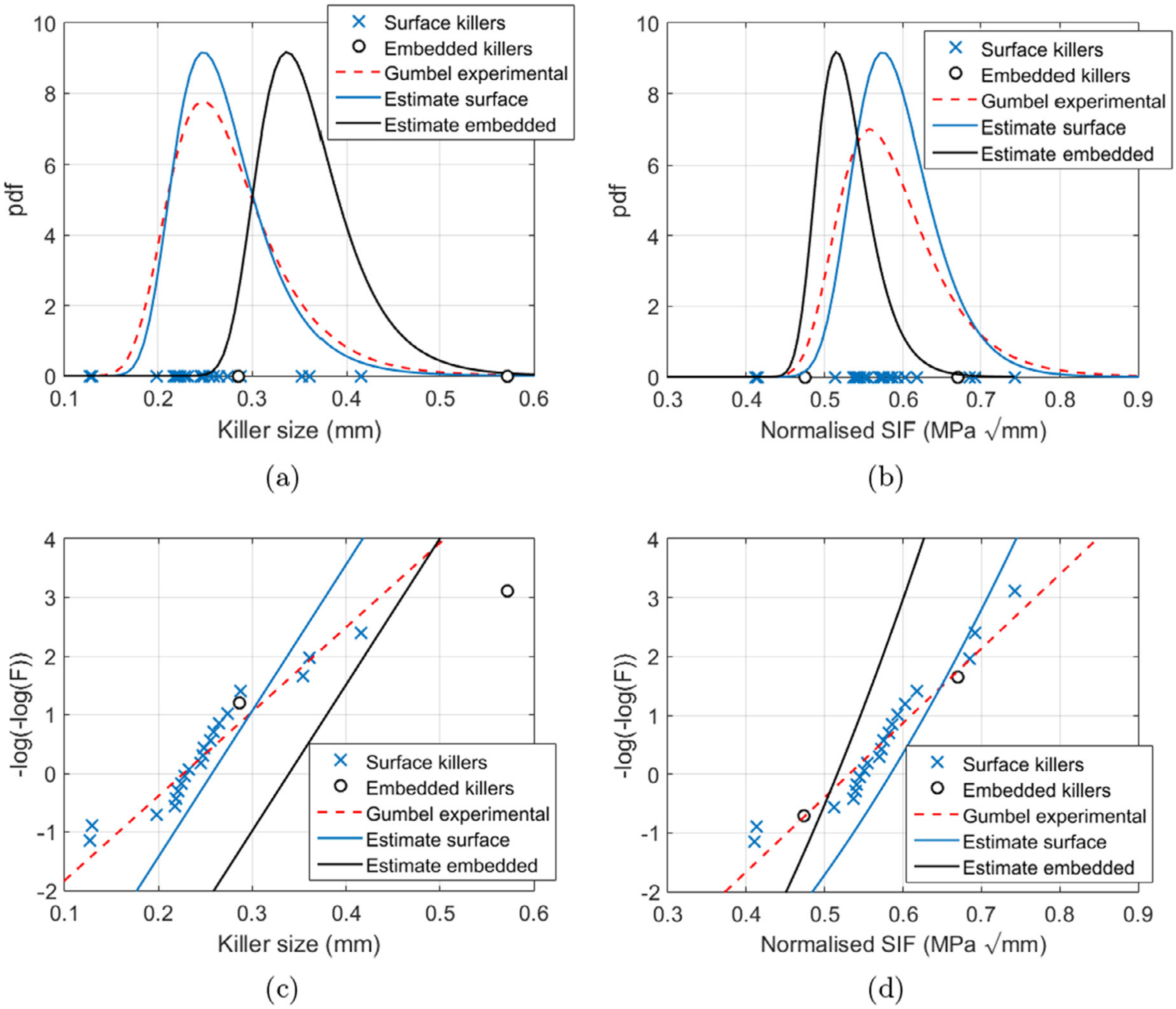

(a) (b) (c) (d)

**Fig. 11.** Extreme value distribution estimate of the maximum defect in $V_{surf}$ and comparison with the defects at the origin of failure considering P1: (a) size and (b) SIF probability distribution, (c) size and (d) SIF distribution in a Gumbel probability plot. The SIF is normalised considering a unitary applied stress.

This analysis (similar results can be also obtained for P2 and P3) explains why failures caused by embedded defects were seen to be unlikely and why they are originated from very large flaws. The failure origin can therefore be described by a probabilistic competing-risk assessment between the maximum SIF distributions in the surface and embedded gauge volumes. Moreover, it is worth reminding that internal cracks (growing in vacuum) generally show lower crack propagation rates than surface cracks [61], which explains why they are rarely found at the origin of failure at high applied stresses.

It is then clear that the SIF is the key parameter for defect criticality and that the size of the critical defects can be predicted using these concepts.

#### 4.2.1. Prediction of defects at the fracture origin

Fig. 7 has shown the strong influence of the killer defect size on the fatigue resistance of the material. Therefore, by knowing the killer defect size distribution, it would be possible to achieve an easy and cheap assessment of the process quality. However, if the estimation of the killer defect size distribution is not an easy task when a complete CT scan of all the parts is available, this is even more complicated in the cases in which performing a proper CT characterisation is not possible. For instance, this could happen when there is no possibility to check all the parts or because some complex shapes cannot be completely scanned with an appropriate resolution.

In these cases, it becomes useful to assess the killer size with a probabilistic approach, performing CT on some representative witness samples [4] and applying statistics of extremes.

The estimation of the maximum defect size in a given volume can be obtained with the usual concepts of *statistics of extremes*, but it is worth adopting the *peak over threshold* (POT) approach in which all the defects above a given threshold size are analysed [8]. The estimate of the killer defect size has to take into account three main variables: (i) the intrinsic vari-

**Table 6**
Determination of equivalent surface volume and important dimensions of the estimated killer size.

| Process | $\bar{a}$ (mm) | $V_{surf}$ (mm$^3$) | $\sqrt{area}_{mean}$ (mm) | $\sqrt{area}_{min}$ (mm) | $\sqrt{area}_{max}$ (mm) |
|---|---|---|---|---|---|
| P1 H | 0.151 | 55 | 0.322 | 0.214 | 0.593 |
| P1 V | 0.150 | 49 | 0.306 | 0.207 | 0.559 |
| P2 H | 0.074 | 27 | 0.130 | 0.085 | 0.206 |
| P2 V | 0.129 | 47 | 0.190 | 0.131 | 0.303 |
| P3 H | 0.063 | 23 | 0.083 | 0.068 | 0.122 |
| P3 V | 0.077 | 29 | 0.088 | 0.081 | 0.117 |

ability of the maximum defect distribution (as a given percentile of the Gumbel distribution); (ii) the orientation of the sample, owing to the anisotropic defect elongation; (iii) the density of the defects over the threshold, which is the main variable introducing scatter between CT measurements performed on the same batch of material.

As most failures start from the surface, the size of the killer defect in a sample can be estimated as the size of the maximum defect in $V_{\text{surf}}$. As depicted in Fig. 10, $V_{\text{surf}}$ has been defined as an external circular crown with a fixed thickness $h$. Considering cylindrical specimens, $V_{surf}$ can be calculated according to Eq. (3), where the thickness $h = \bar{a}/0.8$ is derived from Eq. (2) and $\bar{a}$ is the average experimental radius of the killers measured in the samples.

$$V_{surf} = V_g - V_{int} = \pi \cdot l_g \cdot (r_g^2 - (r_g - h)^2) \tag{3}$$

The average killer size, $\sqrt{area}_{mean}$, was calculated adopting the 50% percentile of the distribution and the average density of the defects exceeding the threshold ($\rho_u$) in a POT maxima sampling [8] in a volume $V_g$. The expected inferior and superior limits, $\sqrt{area}_{min}$ and $\sqrt{area}_{max}$, refer respectively to the 2.5% percentile with minimum $\rho_u$ and 97.5% percentile with maximum $\rho_u$. The results for the processes investigated are summarised in Table 6.

Experimental investigations [62] have shown that subsurface defects in contact or very close to the surface (very small $h$ in Fig. 10a) have the largest SIF. This geometrical problem can be corrected by calculating the *effective defect size* as depicted in Fig. 10b. This can be achieved by applying a multiplication factor of 1.137 to the defect area [62].

The good prediction of the killer size is also confirmed for P2 and P3, as depicted in Fig. 7b. It should be annotated that in the presence of very large defect densities and dimensions some interactions between adjacent defects could occur: this *clustering effect* is not predictable by the proposed model.

This method to estimate the killer defect size is the basis for the determination of the initial crack size in the FCG propagation, which is the topic of Section 5.

## 5. Modelling of fatigue resistance

As introduced in Section 1 and confirmed by the experimental results in Section 3.2, one of the main problems in the fatigue description of AM parts is the large scatter of the experimental results. When the residual stresses are limited and samples are machined, defects are the main variable affecting the fatigue resistance [9,23,63]. Therefore, the largest part of experimental scatter should be strictly related to the initial size of manufacturing defects within the material, which control the lower bound of fatigue resistance [25]. The possibility to predict this scatter from NDE measurements, considering the ability to extrapolate CT scan measurements to large material volumes [8,64], will improve the fatigue assessment and component qualification.

To reach this goal, a model for fatigue strength and life prediction is proposed here. The model can be described in two steps:

1. a suitable description of fatigue strength as the threshold condition for the defects treated as short cracks;
2. a life prediction scheme and its application to the fatigue data of the three processes.

### *5.1. Definition of fatigue strength*

As discussed in the introduction, the presence of manufacturing defects causes a large scatter, especially after the knee-point of the Wöhler curve. Most of this variability can be accounted for defining the relationship between the defect size and the material fatigue strength through the Kitagawa diagram (see [23]). Two of the most used formulations were proposed by Murakami & Endo [65] and El-Haddad [66]. According to Murakami & Endo [65], the threshold for small cracks can be expressed as:

$$\Delta K_{th} \propto (\sqrt{\text{area}})^{1/3} = C_n \tag{4}$$

Applying Eq. (1) in the fatigue strength region, it is possible to substitute $\Delta\sigma_w = \Delta\sigma$ and $\Delta K_{th} = \Delta K$. Equating the crack propagation thresholds defined in Eqs. (1) and (4), the fatigue strength $\Delta\sigma_w$ can be obtained:

$$\Delta\sigma_w = \frac{C_n}{Y \cdot (\sqrt{\text{area}})^{1/6}} \tag{5}$$

where $C_n$ is a parameter that depends on the material hardness and defect position.

Another possibility for describing the Kitagawa diagram is to adopt the *El-Haddad model*, slightly modified as proposed in [67]. According to this formulation, if Eq. (1) is adopted for the SIF, the relationship between the fatigue limit and the defect/crack size can be expressed as:

$$\Delta\sigma_w = \Delta\sigma_{w0} \cdot \sqrt{\frac{\sqrt{\text{area}_0}}{\sqrt{area} + \sqrt{\text{area}_0}}} \tag{6}$$

and:

$$\Delta K_{th} = \Delta K_{th,lc} \cdot \sqrt{\frac{\sqrt{\text{area}}}{\sqrt{\text{area}} + \sqrt{\text{area}_0}}} \tag{7}$$

where

$$\sqrt{area_0} = \frac{1}{\pi}\left(\frac{\Delta K_{th,lc}}{Y \cdot \Delta\sigma_{w0}}\right)^2 \tag{8}$$

is called the *El-Haddad parameter* (expressed with Murakami's $\sqrt{area}$ parameter). The advantage of these formulations is that they describe the smooth transition *short cracks* → *long cracks*, which corresponds to defect sizes $\sqrt{area} > 10\sqrt{area_0}$ [68]. Other models can be applied for modelling the *Kitagawa diagram* (see the review in [69,47]).

The modified El-Haddad's model was in first instance adopted to analyse the fatigue results. All the samples that survived at least $N_{k,\sigma}$ cycles were considered. The introduction of tests on artificial defects (plotted with failures above $N_{k,\sigma}$ and run-outs) helps improving the description in a wider defect size range. The specimens that survived the tests showed no visible damage and were tested again at relatively high stress amplitudes: the size of the defects at the fracture origin in this second test has been adopted to position the run-outs in the Kitagawa diagram.

The fatigue limit in the absence of defects $\Delta\sigma_{w0}$ was estimated as the stress value corresponding to a plastic deformation of 0.05% in the stabilised cyclic curve [70].[1] The long crack propagation threshold at $R = -1$ was initially estimated to be $\Delta K_{th,lc} = 4.1\,MPa\sqrt{m}$ based on the results obtained from the tests on the artificial defects of P1, according to Eq. (1). This value matches with several experimental results obtained for the same material, produced by AM or casting [23].

The parameter $\sqrt{\text{area}_0}$ was finally calculated according to Eq. (8). The best fit is depicted in Fig. 12a. The same diagram is shown in Fig. 12b in terms of crack propagation threshold $\Delta K_{th}$. Note that Fig. 12a is valid only for surface cracks, as the applied stress should be rescaled when dealing with embedded killers. In Fig. 12b, however, the different position is already accounted for by the $Y$ term in the SIF assessment. Therefore, the embedded defects are also described by a unique Kitagawa diagram: this confirms the previous results of Section 4.2, i.e., that the SIF at the defect is the parameter controlling the fatigue strength/life.

Fig. 12a also shows that the data on natural and artificial defects can be fitted with a slope $1:6$, as predicted by the Murakami-Endo model [65]. This model can predict results similar to the models for strength based on $\Delta J_{eff}$ [47]. The reason for showing only the El-Haddad model is that this is the basis for the life prediction model described in Section 5.2.

The result of the analysis for the P1 process show a non-negligible intrinsic scatter, which can be due to several factors (e.g., heterogeneous microstructure, anisotropy, residual stresses, errors in testing, and defect size measurements). The resulting coefficient of variation is in the order of 8–10% for $\Delta\sigma_{w0}$ and $\Delta K_{th,lc}$. As for P2 and P3, two slightly different Kitagawa diagrams were obtained, as depicted in Fig. 12c. As expected, there are slight differences between the processes, owing to the fact that a finer and more homogeneous microstructure tends to increase $\Delta\sigma_{w0}$ and decrease $\Delta K_{th,lc}$, as measured by the CPCA experiments (see Section 3.3).

It is of some importance, for the sake of life prediction, to remark that the fatigue limits for P1-P3 corresponds to stress levels above $1/3 \cdot \sigma_{wo}$, which is the limit of applicability of linear elastic fracture mechanics (LEFM) [70]. This implies that the contribution of *cyclic plasticity* has to be considered for the driving force in the life prediction.

Finally, Fig. 13 depicts the fatigue results of the three processes, normalising the applied stress with respect to the fatigue strength $\Delta\sigma_w$ defined by the Kitagawa diagram for the particular size of the killer defect found in every sample. From this picture, it can clearly be seen that all the data collapse and follow the same trend, stabilising around 1 over $2 \cdot 10^5$ cycles. In fact, all the data points over this value can be described by a normal distribution with standard deviation of 0.13. Therefore, the resulting coefficient of variation is of the order of 13%. This value is very low, considering the enormous dispersion shown in the S-N diagram of Fig. 7a, but it still has a non-negligible influence in a probabilistic assessment during the design phase. This variability can be explained by microstructural effects affecting crack nucleation and propagation and the other

---

[1] Note that $\Delta\sigma_{w0}$ represents the fatigue limit in absence of defects, and it is therefore a theoretical limit for a material. However, for small defects there are significant microstructural effects. This makes it possible to say that the characteristic *microstructural size* is the upper bound for the application of *mechanical models* such as those considered here [71].

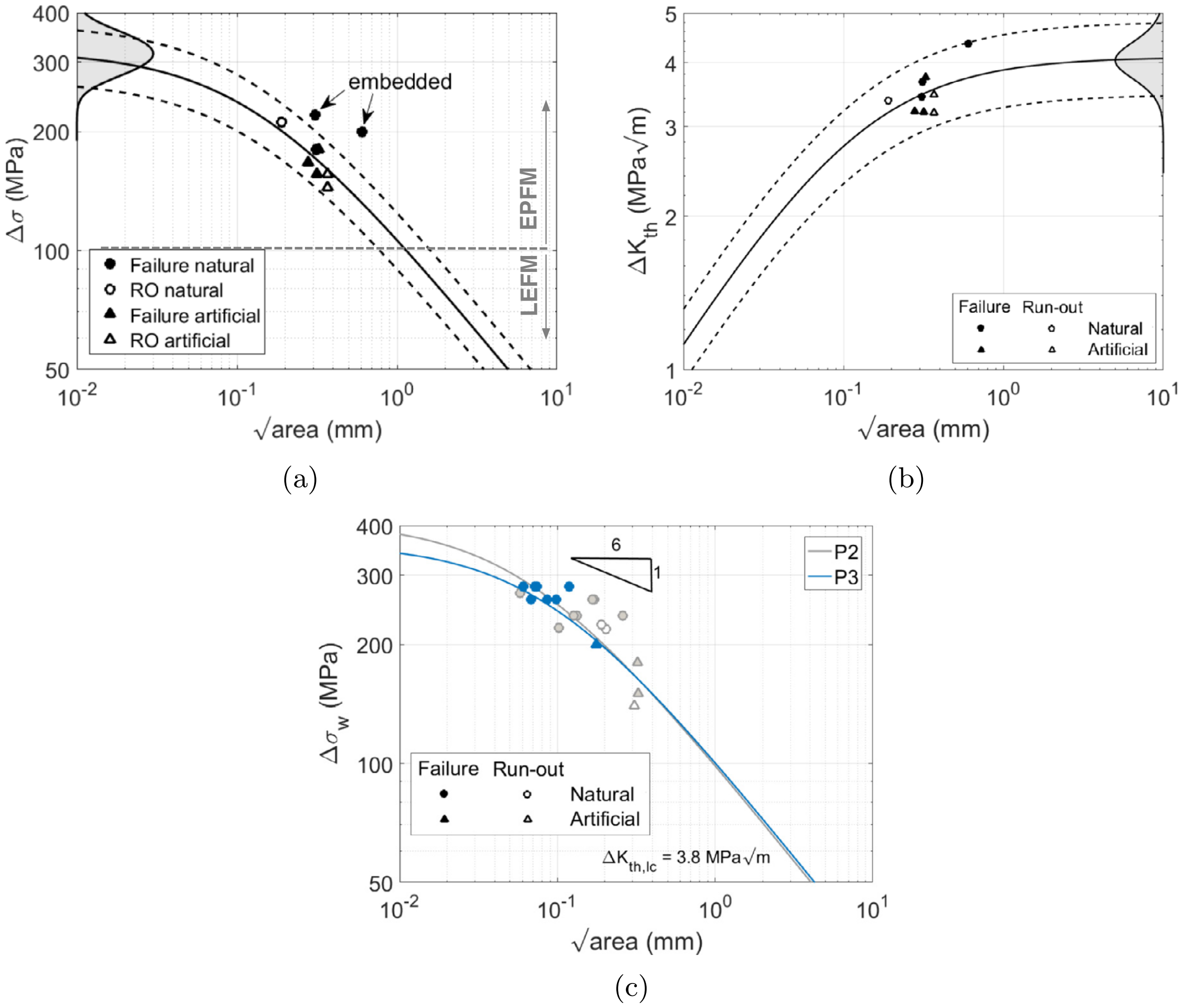

(a) (b)

(c)

**Fig. 12.** Kitagawa diagram obtained by HCF tests on P1, fitted by El-Haddad's formulation: (a) $\Delta\sigma_w$ vs $\sqrt{area}$ for P1, (b) $\Delta K_{th}$ vs $\sqrt{area}$ for P1; (c) $\Delta\sigma_w$ vs $\sqrt{area}$ for P2 and P3.

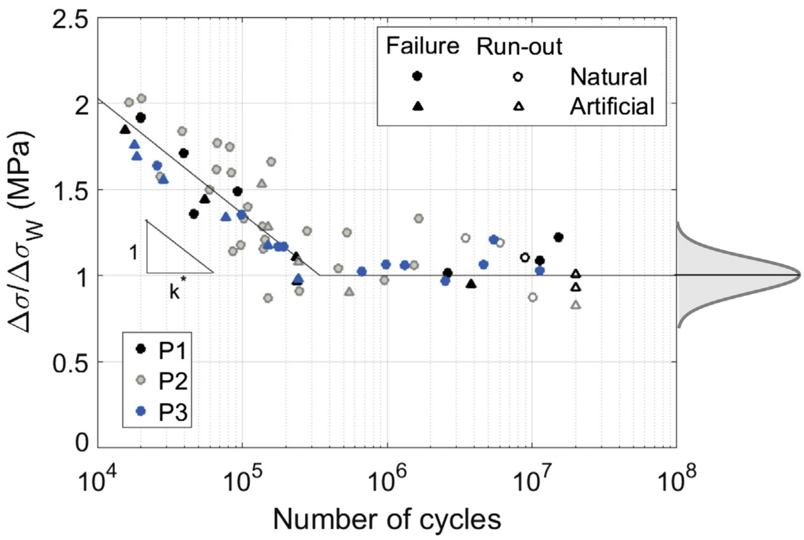

**Fig. 13.** S-N data for the three processes normalised by the correspondent fatigue strength resistance, as in Fig. 12.

errors during experiments (e.g., residual stresses and defect size measurement). It is also worth noting that the scatter band of the $\Delta\sigma/\Delta\sigma_w$ is somewhat larger than the typical value of 5% obtained for other cases (e.g., inclusions in high-strength steels [25]).

### *5.2. Fracture mechanics-based prediction of the S-N curves*

#### *5.2.1. Initial crack size*

Most of AM defects are voids (porosity, lack of fusion, shrinkage) or inclusions. When dealing with fatigue problems, these become nucleation sites for short fatigue cracks. In Section 4.2, it was demonstrated that the failure happens in correspondence with the defect having the maximum SIF, which is almost certainly surface or subsurface. At the same time, it has been shown that the size of the killer defects can be estimated on the basis of X-ray CT data by applying the concepts of statistics of extremes described by the authors and applied to P1 [8]. As discussed in Section 4.2, the main sources of variability associated with the maximum defect size in a given material volume are the intrinsic scatter (expressed by the percentile of the extreme value distribution), the defect density, and the orientation of the samples.

To calculate the initial size of the cracks, the shape of the surface defects is approximated with a semi-circle. The initial crack depth $a_i$ depends on the killer size $\sqrt{area_i}$ according to the relation reported in Eq. (9):

$$a_i = \sqrt{area_i} \cdot \sqrt{2/\pi} \tag{9}$$

The determination of $\sqrt{area_i}$ has already been discussed in Section 4.2 and the values are reported in Table 6. Referring to a gauge volume, three dimensions of the initial crack size were obtained, which describe the average value and the range of the expected crack size:

- $a_{min}$: obtained adopting the minimum $\sqrt{area_{min}}$ of the process;
- $a_{mean}$: obtained adopting $\sqrt{area_{mean}}$ of the process;
- $a_{max}$: obtained adopting the maximum $\sqrt{\text{area}_{max}}$ of the process.

#### *5.2.2. Crack growth models*

Fatigue crack growth simulations have been performed using both the software Nasgro 4.0/ESACRACK and a crack propagation algorithm developed for this project. The stress intensity factor was calculated by adopting the standard solution for a surface crack propagating in a rod [72], the crack size being described only by its depth $a_i$, as discussed in Section 5.2.1. The diameter of the rod equals that of the investigated sample gauge length.

The $\Delta K - da/dN$ curve was described by a NASGRO-type equation (Eq. (10)), whose parameters were derived by FCG tests at $R = 0.7$ on P2:

$$\frac{da}{dN} = C\left[\left(\frac{1-f_N}{1-R}\right)\Delta K\right]^n \left(1-\frac{\Delta K_{th}}{\Delta K}\right)^p \tag{10}$$

where $f_N$ is the *Newman's closure function*, which is able to describe the crack closure at different stress ratios [54]:

$$f_N = \frac{\sigma_{op}}{\sigma_{max}} = f(\alpha, R, \sigma_{max}/\sigma_o) \tag{11}$$

The flow stress $\sigma_0$ was calculated as the average between the static ultimate tensile stress and the yield stress. Similar slopes in the Wöhler curves of the batches, together with the results of Fig. 13, suggest that the FCG properties should not be remarkably different, and thus, the same equation has also been adopted for P1 and P3. The dependence of $\Delta K_{th}$ on the crack size was expressed with Eq. (7), modified as in Eq. (9) to account for the crack size.

Life prediction was carried out by applying different options:

#1 – the standard assumptions in ESACRACK/NASGRO/AFGROW: $\sigma_{max}/\sigma_0 = 0.3$, constraint factor $\alpha = 1.9$ and $\sqrt{area_0} = 0.038$ mm;
#2 – the real applied $\sigma_{max}/\sigma_o$ and $\sqrt{area_0}$ estimated as described in Section 5.1;
#3 – elastic simulation considering a *plasticity-corrected* crack length for calculating $\Delta K$ in Eq. (10) with a formulation of the type:

$$a_p = a + \beta \cdot r_p \tag{12}$$

where $r_p$ is the plastic radius ahead of the crack tip and $\beta$ was determined with a series of preliminary analyses [73], such that the growth rate at higher stress levels became comparable with estimations based on the *PJ* approach [74,75].

The results of the simulations for P1 considering an initial crack size equivalent to the maximum defect (97.5% percentile) are depicted in Fig. 14a and they clearly show that conventional LEFM assumptions (#1) do not provide good results. Using option #2, the slope of the curve for high applied stresses increases owing to the improved definition of the opening stress, whereas the fatigue strength at 10 million cycles becomes more conservative and closer to the lower bound of the artificial

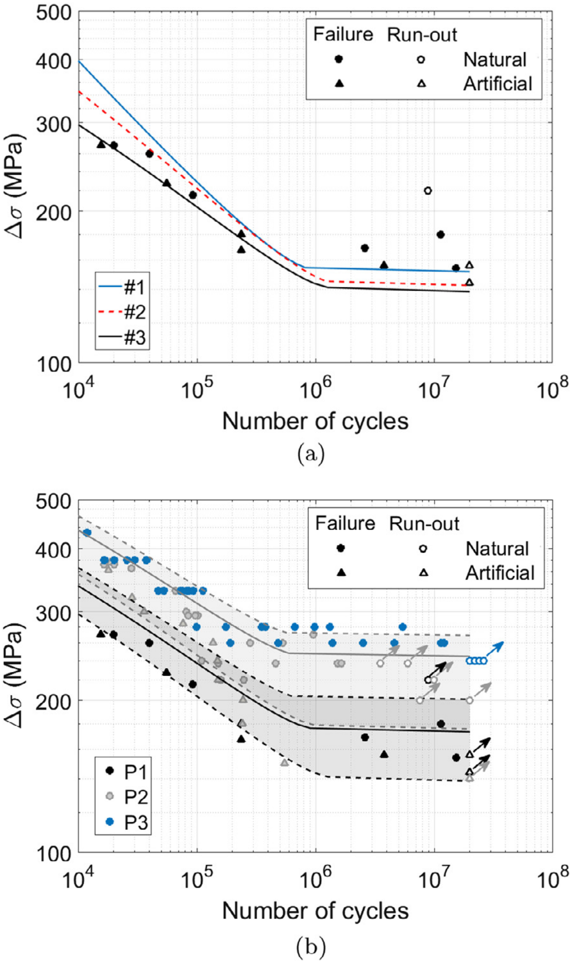

**Fig. 14.** Fatigue life estimates: (a) lower bound for P1 adopting the three options presented, (b) option #3 applied to batches P1 and P2 with their 95% scatter band.

data. Eventually, option #3 provides a good description of the slope, with an estimated value $k_\sigma = 6.1$ very close to the experimental results. This highlights the importance of the *elastoplastic* conditions for a correct analysis of the AM defects.

Fig. 14b shows the results for processes P1 and P2, considering the simulation scheme #3. The dispersion of the data has been assessed by selecting the three initial crack sizes described in Section 5.2.1. The results confirm a good prediction, together with a clear demonstration that the defect size is the key factor affecting the fatigue properties of machined specimens of AlSi10Mg manufactured by AM. The simulations for P3 are not shown, because they would overlap with the upper part of the P2 scatter band.

## 6. Outlook

### 6.1. Subsurface defects

A peculiar feature of as-built AM parts is the presence of diffused porosity in the subsurface region [9,21], particularly pronounced in downfacing inclined parts [23] where the surface quality is understandably lower (see Fig. 15a and b). This type of feature explains very well the dramatic reduction in fatigue strength due to the *as built surface*, which cannot be avoided with a simple polishing [76] but rather with a process (e.g., machining, chemical milling) able to remove the external surface layers [9].

Even if the single pores have dimensions which are too which is too small to influence the fatigue resistance, the large pore density in this region creates very dangerous *clusters*, resulting in a weak subsurface area. Considering also this problem also in terms of *equivalent defects*, this *belt* of pores can be approximated as a 2D surface crack with a

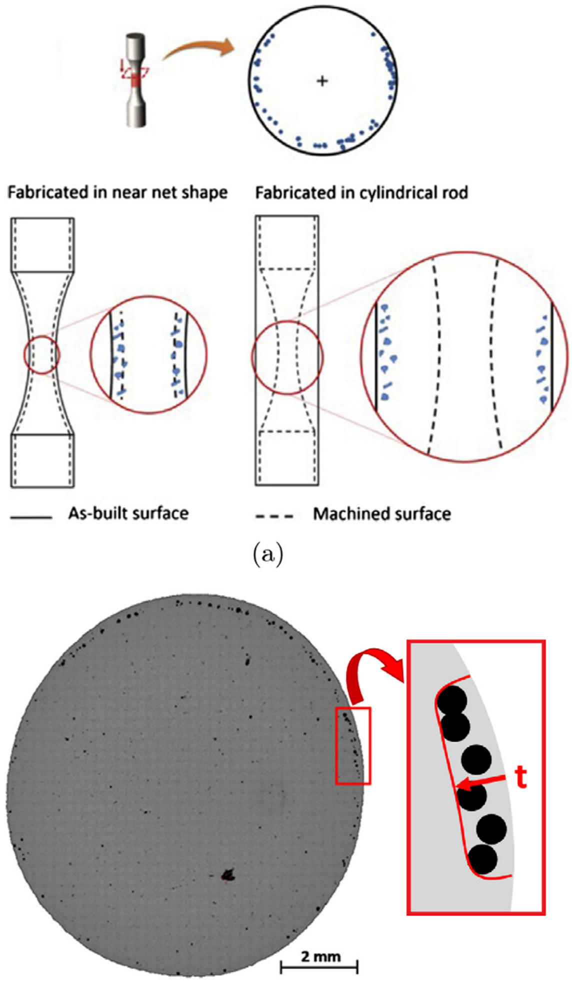

(a)

(b)

**Fig. 15.** Typical subsurface features in AB parts: (a) subsurface porosity (from [9] with permission of the authors), (b) subsurface porosity in the downfacing region of inclined AlSi10Mg parts (from [23]) and scheme for equivalent defect size definition.

depth *t*, which is approximately 200–250 μm in Fig. 15b. For this type of geometry, the $\sqrt{\text{area}}$ can be calculated effective as in Eq. (13) [25]:

$$\sqrt{\text{area}}_{eff} \simeq t \cdot \sqrt{10} \tag{13}$$

where *t* is the maximum depth reached by the pores (see a sketch in Fig. 15b).

### 6.2. Probabilistic concepts

We have here proposed a simple life prediction scheme based on the *major* source of scatter, which are the defects. However, there are other sources of variability apart from the initial crack size (e.g., fatigue crack growth curve and intrinsic material scatter) that lead to the dispersion shown in Fig. 14b.

In the framework of a comprehensive probabilistic assessment, this scatter can be described as an *intrinsic variability* of the Kitagawa diagram (or the fatigue strength model) [77] for fatigue strength, or it would need a full probabilistic approach for propagation considering a variability for $\Delta K_{th}$ consistent with the previously discussed 10% scatter.

A new probabilistic framework can be also developed to take into account the different variabilities considered so far (distribution of defects, defect density, and intrinsic variability of the threshold model) [78,79]. In this framework, the final fatigue assessment becomes a competing risk between surface and internal defects, as well as clusters of subsurface porosity and poor surface roughness, which can be described by defining an *equivalent initial flaw size* [80,81,53].

## 7. Conclusions

This study has summarised the results related to a fatigue testing campaign on AlSi10Mg produced by SLM, considering three slightly different processes. A model for estimating fatigue life and strength considering the influence of manufacturing defects has been proposed. The significant results of the analysis are:

- the evolution of the SLM process in the last two years have significantly improved the quality and fatigue resistance of the material investigated, which outperforms the properties of cast material;
- the material has been comprehensively characterised (X-ray CT, static, FCG, HCF, and LCF). The fatigue resistance is mainly controlled by manufacturing defects, such as porosity and lack of fusion;
- a lower bound S-N curve can be defined by introducing artificial defects with a size calculated as a safe percentile of the maximum defect distribution within the gauge volume;
- the fatigue strength in the presence of defects and small crack propagation threshold have been defined by the Kitagawa diagram with natural and artificial defects;
- a criterion based on SIF assessment for the definition of the most detrimental defect from those detected by CT has been proposed and validated using experimental results;
- a model for fatigue life estimation in the HCF regimes has been proposed, which can describe the experimental scatter by evaluating the distribution of the initial defect size in the surface gauge volume of the samples;
- the application of fracture mechanics yields good results, keeping in mind that the effect of plasticity is non-negligible.

## Acknowledgements

The activity of S. Romano has been supported by ESA through the Networking Partnering Initiative (NPI). We acknowledge the support of RUAG, in particular M. Gschweitl, for manufacturing the specimens and for permission to publish results of this long-term research activity. We are also indebted to J. Bennet (STFC; Harvell) for his fractography support and to B. Zielinski (University of Kassel, Physics Department) for manufacturing the microdefects by the special technique developed at Kassel University.

S. Romano is especially grateful to the *Kassel group* (J. Steger, M. Wicke, M. Lütje, F. Zeismann), who helped him during his visit at Kassel University.

Contributions to the paper are: (i) S. Romano performed the tests at Polimi together with analyses and contributed to writing the paper; (ii) A. Brandão took care of the CT scans; (iii) J. Gumpinger took care of the fatigue tests in ESA and contributed to the manuscript; (iv) A. Brückner-Foit directed the tests at Kassel; (v) T. Ghidini directed the test program of ESA, to which the tests on P1 and P3 belong; (vi) S. Beretta directed this research on defect-based analysis, elaborated the models and took care of the manuscript.

## References

[1] Moriaux F. Additive manufacturing for space application; 2015. <https://speakerdeck.com/altairhyperworks/additive-manufacturing-for-space-application-franck-mouriaux-ruag-space>.

[2] U.S. Department of Transportation. FAA Advisory Circular 25. 1309-1A System Design and Analysis; 1988.

[3] U.S. Department of Transportation. FAA Advisory Circular 33.70-1. Guidance Material for Aircraft Engine Life-Limited Parts Requirements; 2009.

[4] National Aeronautics and Space Administration (NASA). EM20 – Engineering and Quality Standard for Additively Manufactured Spaceflight Hardware (draft). Tech. rep.; 2015.

[5] Seifi M, Salem A, Satko D, Shaffer J, Lewandowski JJ. Defect distribution and microstructure heterogeneity effects on fracture resistance and fatigue behavior of EBM Ti-6Al-4V. Int J Fatigue 2017;94:263–87. doi: https://doi.org/10.1016/j.ijfatigue.2016.06.001.

[6] Gorelik M. Additive manufacturing in the context of structural integrity. Int J Fatigue 2017;94:168–77. doi: https://doi.org/10.1016/j.ijfatigue.2016.07.005.

[7] Seifi M, Salem A, Beuth J, Harrysson O, Lewandowski JJ. Overview of materials qualification needs for metal additive manufacturing. Jom 2016;68(3):747–64. doi: https://doi.org/10.1007/s11837-015-1810-0.

[8] Romano S, Brandão A, Gumpinger J, Gschweitl M, Beretta S. Qualification of AM parts: extreme value statistics applied to tomographic measurements. Mater Des 2017:1–34.

[9] Yadollahi A, Shamsaei N. Additive manufacturing of fatigue resistant materials: challenges and opportunities. Int J Fatigue 2017;98(January):14–31. doi: https://doi.org/10.1016/j.ijfatigue.2017.01.001.

[10] Mower TM, Long MJ. Mechanical behavior of additive manufactured, powder-bed laser-fused materials. Mater Sci Eng A 2015;651:198–213. doi: https://doi.org/10.1016/j.msea.2015.10.068.

[11] Mardaras J, Emile P, Santgerma A. Airbus approach for F&DT stress justification of additive manufacturing parts. In: Third international symposium on fatigue design and material defects (FDMD3), Lecco; 2017.

[12] Persenot T, Buffière J-Y, Maire E, Dendievel R, Martin G. Fatigue properties of EBM as-built and chemically etched thin parts. In: Fatigue design and material defects (FDMD), no; September, 2017.

[13] Brandão A, Gumpinger J, Gschweitl M, Hofbauer P, Ghidini T. Fatigue properties of additively manufactured AlSi10Mg – surface treatment effect. In: Third international symposium on fatigue design and material defects (FDMD3), Lecco; 2017.

[14] Mohammad A, Mohammed MK, Alahmari AM. Effect of laser ablation parameters on surface improvement of electron beam melted parts. Int J Adv Manuf Technol 2016;87(1):1033–44. doi: https://doi.org/10.1007/s00170-016-8533-4.

[15] Król M, Dobrzański LA, Reimann L, Czaja I. Surface quality in selective laser melting of metal powders. Arch Mater Sci 2013;60(2):87–92.

[16] Klingvall Ek R, Rännar L-E, Bäckstöm M, Carlsson P. The effect of EBM process parameters upon surface roughness. Rapid Prototyp J 2016;22(3):495–503. doi: https://doi.org/10.1108/RPJ-10-2013-0102.

[17] Siddique S, Imran M, Walther F. Very high cycle fatigue and fatigue crack propagation behavior of selective laser melted AlSi12 alloy. Int J Fatigue 2017;94:246–54.
[18] Siddique S, Imran M, Rauer M, Kaloudis M, Wycisk E, Emmelmann C, et al. Computed tomography for characterization of fatigue performance of selective laser melted parts. Mater Des 2015;83:661–9. doi: https://doi.org/10.1016/j.matdes.2015.06.063.
[19] Fatemi A, Molaei R, Sharifimehr S, Phan N, Shamsaei N. Multiaxial fatigue behavior of wrought and additive manufactured ti-6al-4v including surface finish effect. Int J Fatigue 2017;100:347–66.
[20] Wycisk E, Emmelmann C, Siddique S, Walther F. High Cycle Fatigue (HCF) performance of Ti-6Al-4V alloy processed by selective laser melting. Adv Mater Res 2013;816–817:134–9. doi: https://doi.org/10.4028/www.scientific.net/AMR.816-817.134.
[21] Edwards P, Ramulu M. Fatigue performance evaluation of selective laser melted Ti-6Al-4V. Mater Sci Eng A 2014;598:327–37. doi: https://doi.org/10.1016/j.msea.2014.01.041.
[22] Brandão A, Gerard R, Gumpinger J, Ghidini T. X-ray CT and fatigue investigations on additive manufactured materials. In: Techinical interchang. meet. ESTEC, Noordwijk, NL; 2015.
[23] Beretta S, Romano S. A comparison of fatigue strength sensitivity to defects for materials manufactured by AM or traditional processes. Int J Fatigue (Spec Additive Manuf) 2017;94:178–91.
[24] Kitagawa H, Takahashi S. Applicability of fracture mechanics to very small cracks or the cracks in the early stage. In: Proc. 2nd int. conf. mech. behaviour of materials – ICM2; 1976. p. 627–31.
[25] Murakami Y. Metal fatigue: effects of small defects and nonmetallic inclusions. Oxford: Elsevier; 2002.
[26] Brandl E, Heckenberger U, Holzinger V, Buchbinder D. Additive manufactured AlSi10Mg samples using Selective Laser Melting (SLM): microstructure, high cycle fatigue, and fracture behavior. Mater Des 2012;34:159–69. doi: https://doi.org/10.1016/j.matdes.2011.07.067.
[27] Buchbinder D, Meiners W. Generative Fertigung von Aluminiumbauteilen für die Serienproduktion. Tech. rep. Fraunhofer Institute; 2011.
[28] Maskery I, Aboulkhair NT, Tuck C, Wildman RD, Ashcroft IA, Everitt NM, et al. Fatigue performance enhancement of selectively laser melted aluminium alloy by heat treatment. Solid Free Fabr Symp 2015:1017–25.
[29] Peralta AD, Enright M, Megahed M, Gong J, Roybal M, Craig J. Towards rapid qualification of powder-bed laser additively manufactured parts. Integr Mater Manuf Innov 2016;5(1):1–23. doi: https://doi.org/10.1186/s40192-016-0052-5.
[30] Murakami Y. Inclusion rating by statistics of extreme values and its application to fatigue strength prediction and quality control of materials. J Res Natl Inst Stand Tehcnol 1994;99:345–51.
[31] Murakami Y, Beretta S. Small defects and inhomogeneities in fatigue strength: experiments, models and statistical implications. Extremes 1999;2 (2):123–47. doi: https://doi.org/10.1023/A:1009976418553.
[32] `ASTM E2283-03`. Standard practice for extreme value analysis of nonmetallic inclusions in steels and other microstructural features. American Society for Testing And Materials; 2003.
[33] Thijs L, Kempen K, Kruth JP, Van Humbeeck J. Fine-structured aluminium products with controllable texture by selective laser melting of pre-alloyed AlSi10Mg powder. Acta Mater 2013;61(5):1809–19. doi: https://doi.org/10.1016/j.actamat.2012.11.052.
[34] Chen B, Moon SK, Yao X, Bi G, Shen J, Umeda J, et al. Strength and strain hardening of a selective laser melted AlSi10Mg alloy. Scripta Mater 2017;141:45–9. doi: https://doi.org/10.1016/j.scriptamat.2017.07.025.
[35] Lewandowski JJ, Seifi M. Metal additive manufacturing: a review of mechanical properties. Annu Rev Mater Res 2016;46(1):151–86. doi: https://doi.org/10.1146/annurev-matsci-070115-032024.
[36] Volume Graphics. VGStudio MAX 2.2 Reference Manual; 2012.
[37] Murakami Y, Nemat-Nasser S. Growth and stability of interacting surface flaws of arbitrary shape. Eng Fract Mech 1983;17(3):193–210. doi: https://doi.org/10.1016/0013-7944(83)90027-9.
[38] ISO 6892-1. Metallic materials – tensile testing – Part 1: method of a test at room temperature; 2009.
[39] Ramberg W, Osgood WR. Description of stress-strain curves by three parameters. Tech. rep. Washington, DC, United States: National Advisory Committee for Aeronautics; 1943.
[40] Romano S, Beretta S, Foletti S. LCF response of AlSi10Mg obtained by additive manufacturing. In: Eighth international conference on low cycle fatigue (LCF8), Dresden; 2017.
[41] ASTM E606. Standard Test Method for Strain-Controlled Fatigue Testing; 2004. https://doi.org/10.1520/E0606-04E01.
[42] Bode B, Wessel W, Brueckner-Foit A, Mildner J, Wollenhaupt M, Baumert T. Local deformation at micro-notches and crack initiation in an intermetallic c-TiAl-alloy. Fatigue Fract Eng Mater Struct 2016;39(2):227–37. doi: https://doi.org/10.1111/ffe.12356.
[43] A. WK49229. New guide for anisotropy effects in mechanical properties of am parts. West Conshohocken, PA: ASTM International.
[44] ASTM E647. Standard Test Method for Measurement of Fatigue Crack Growth Rates. https://doi.org/10.1520/E0647-13A.2.
[45] Newman J, Yamada Y. Compression precracking methods to generate near-threshold fatigue-crack-growth-rate data. Int J Fatigue 2010;32(6):879–85.
[46] Tanaka K, Akiniwa Y. Resistance-curve method for predicting propagation threshold of short fatigue cracks at notches. Eng Fract Mech 1988;30 (6):863–76. doi: https://doi.org/10.1016/0013-7944(88)90146-4. URL <http://linkinghub.elsevier.com/retrieve/pii/0013794488901464> .
[47] Zerbst U, Vormwald M, Pippan R, Gänser H-P, Sarrazin-Baudoux C, Madia M. About the fatigue crack propagation threshold of metals as a design criterion–a review. Eng Fract Mech 2016;153:190–243.
[48] Tabernig B, Pippan R. Determination of the length dependence of the threshold for fatigue crack propagation. Eng Fract Mech 2002;69(8):899–907. doi: https://doi.org/10.1016/S0013-7944(01)00129-1. URL <http://linkinghub.elsevier.com/retrieve/pii/S0013794401001291> .
[49] Pippan R, Berger M, Stüwe HP. The influence of crack length on fatigue crack growth in deep sharp notches. Metall Trans A 1987;18(4):429–35. doi: https://doi.org/10.1007/BF02648804. URL <http://link.springer.com/10.1007/BF02648804> .
[50] Sames WJ, List FA, Pannala S, Dehoff RR, Babu SS. The metallurgy and processing science of metal additive manufacturing. Int Mater Rev 2016;61 (5):315–60. doi: https://doi.org/10.1080/09506608.2015.1116649. URL <http://www.tandfonline.com/doi/full/10.1080/09506608.2015.1116649> .
[51] Maskery I, Aboulkhair NT, Corfield MR, Tuck C, Clare AT, Leach RK, et al. Quantification and characterisation of porosity in selectively laser melted Al-Si10-Mg using X-ray computed tomography. Mater Charact 2016;111:193–204. doi: https://doi.org/10.1016/j.matchar.2015.12.001.
[52] Khairallah SA, Anderson AT, Rubenchik A, King WE. Laser powder-bed fusion additive manufacturing: physics of complex melt flow and formation mechanisms of pores, spatter, and denudation zones. Acta Mater 2016;108:36–45.
[53] Masuo H, Tanaka Y, Morokoshi S, Yagura H, Uchida T, Yamamoto Y, et al. Effect of defects, surface roughness and HIP on fatigue strength of Ti-6Al-4V manufactured by additive manufacturing. In: Third international symposium on fatigue design and material defects (FDMD3), Lecco; 2017.
[54] Newman JC. Jr. A crack opening stress equation for fatigue crack growth. Int J Fract 1984;24(4):131–5.
[55] Pippan R, Riemelmoser F. 4.07 – modeling of fatigue crack growth: dislocation models. In: Milne I, Ritchie R, Karihaloo B, editors. Comprehensive structural integrity, Pergamon, Oxford; 2003. p. 191–207. https://doi.org/10.1016/B0-08-043749-4/04035-0.
[56] Hertzberg RW. On the calculation of closure-free fatigue crack propagation data in monolithic metal alloys. Mater Sci Eng: A 1995;190(1–2):25–32. doi: https://doi.org/10.1016/0921-5093(94)09610-9. URL <http://linkinghub.elsevier.com/retrieve/pii/0921509394096109> .
[57] FKM Guideline. Analytical strength assessment of components in mechanical engineering. 6th ed. VDMA-Verl; 2012.
[58] Sonsino CM. Course of SN-curves especially in the high-cycle fatigue regime with regard to component design and safety. Int J Fatigue 2007;29:2246–58. doi: https://doi.org/10.1016/j.ijfatigue.2006.11.015.
[59] Sonsino CM, Franz R. Multiaxial fatigue assessment for automotive safety components of cast aluminium EN AC-42000 T6 (G-AlSi7Mg0.3 T6) under constant and variable amplitude loading. Int J Fatigue 2017;100:489–501. doi: https://doi.org/10.1016/j.ijfatigue.2016.10.027.
[60] Murakami Y, Isida M. Analysis of arbitrarily shaped surface crack and stress field at crack front near surface. Trans Jap Soc Mech Eng Ser A 1985;51:1050–6.

[61] Serrano-Munoz I, Buffiere J-Y, Mokso R, Verdu C, Nadot Y. Location, location & size: defects close to surfaces dominate fatigue crack initiation. Scientific Reports 2017;7(45239):1–9. http://10.0.4.14/srep45239. https://doi.org/10.1038/srep45239.

[62] Murakami Y, Matsunaga H. Effect of small defects on Fatigue strength of Ti-6Al-4V: the final report for AGUSTA. Tech. rep. Fukuoka, Japan: Kyushu University; 2002.

[63] Leuders S, Thöne M, Riemer A, Niendorf T, Tröster T, Richard HA, et al. On the mechanical behaviour of titanium alloy TiAl6V4 manufactured by selective laser melting: fatigue resistance and crack growth performance. Int J Fatigue 2013;48:300–7. doi: https://doi.org/10.1016/j.ijfatigue.2012.11.011.

[64] Romano S, Beretta S, Cova M. Quality control of cast iron: extreme value statistics applied to CT measurements. In: Third international symposium on fatigue design and material defects (FDMD3), Lecco; 2017.

[65] Murakami Y, Endo M, Effect of hardness and crack geometries on $\Delta K_{th}$ of small cracks emanating from small defects. In: Miller K, Rios EDL, Editors. The Behaviour of short fatigue cracks. MEP; 1986.

[66] El Haddad MH, Topper TH, Smith KN. Prediction of non propagating cracks. Eng Fract Mech 1979;11(3):573–84. doi: https://doi.org/10.1016/0013-7944(79)90081-X.

[67] Beretta S, Carboni M, Madia M. Modelling of fatigue thresholds for small cracks in a mild steel by "strip-yield" model. Eng Fract Mech 2009;76 (10):1548–61.

[68] Suresh S, Ritchie RO. Propagation of short fatigue cracks. Int Met Rev 1984;29(6):445–76. doi: https://doi.org/10.1179/imtr.1984.29.1.445.

[69] Murakami Y, Endo M. Effect of defects, inclusions and inhomogeneities on fatigue strength. Int J Fatigue 1994;16:163–82.

[70] Miller K. The short crack problem. Fatigue Fract Eng Mater Struct 1982;5(3):223–32.

[71] Miller K. The two thresholds of fatigue behaviour. Fatigue Fract Eng Mater Struct 1993;16(9):931–9.

[72] Forman RG, Shivakumar V. Growth behavior of surface cracks in the circumferential plane of solid and hollow cylinders; 1986. p. 59–74.

[73] Newman J, Phillips EP, Swain M. Fatigue-life prediction methodology using small-crack theory. Int J Fatigue 1999;21(2):109–19.

[74] Vormwald M, Seeger T. The consequences of short crack closure on fatigue crack growth under variable amplitude loading. Fatigue Fract Eng Mater Struct 1991;14(2/3):205–25.

[75] Vormwald M. Elastic-plastic fatigue crack growth. In: Adv. methods fatigue assess. Berlin, Heidelberg: springer; 2013. p. 391–481.

[76] Konečná R, Nicoletto G, Fintova S, Frkàň M. As-built surface layer characterization and fatigue behavior of DMLS Ti6Al4V. In: Third international symposium on fatigue design and material defects (FDMD3), Lecco; 2017.

[77] Liu Y, Mahadevan S. Probabilistic fatigue life prediction using an equivalent initial flaw size distribution. Int J Fatigue 2009;31(3):476–87.

[78] Romano S, Beretta S. Fatigue assessment of AM parts: a new computational framework based on CT scans. In: Symp. struct. durab. Darmstadt, Darmstadt; 2017.

[79] Romano S, Miccoli S, Beretta S. FE-based probabilistic analysis for fatigue assessment of AM parts. In: 1st ECCOMAS thematic conference on simulation for additive manufacturing, Munich; 2017.

[80] Greitemeier D, Dalle Donne C, Syassen F, Eufinger J, Melz T. Effect of surface roughness on fatigue performance of additive manufactured Ti-6Al-4V. Mater Sci Technol 2016;32(7):629–34. doi: https://doi.org/10.1179/1743284715Y.0000000053.

[81] Grandt AFJ. Fundamentals of structural integrity: damage tolerant design and nondestructive evaluation. J. Wiley; 2003.